AD-A262 052

⑫

DOCUMENTATION PAGE

Form Approved
OMB No 0704 0188

Unclassified	1b RESTRICTIVE MARKINGS
2a SECURITY CLASSIFICATION AUTHORITY	3 DISTRIBUTION / AVAILABILITY
2b DECLASSIFICATION / DOWNGRADING SCHEDULE	Approved for public release; Distribution Unlimited

93-04218

4 PERFORMING ORGANIZATION REPORT NUMBER(S)	5 MONITORING OI

6a NAME OF PERFORMING ORGANIZATION	6b OFFICE SYMBOL (If applicable)	7a NAME OF MONITORING ORGANIZATION
Center for Mat.Sci.& Engr. The University of Texas		Office of Naval Research

6c ADDRESS (City, State, and ZIP Code)	7b ADDRESS (City, State, and ZIP Code)
The Center for Materials Science & Engineering The University of Texas at Austin Austin, TX 78712	800 N. Quincy Street Arlington, VA 22217-5000

8a NAME OF FUNDING / SPONSORING ORGANIZATION	8b OFFICE SYMBOL (If applicable)	9 PROCUREMENT INSTRUMENT IDENTIFICATION NUMBER
Office of Naval Research		N00014-90-J-1164

8c ADDRESS (City, State, and ZIP Code)	10 SOURCE OF FUNDING NUMBERS			
	PROGRAM ELEMENT NO	PROJECT NO	TASK NO	WORK UNIT ACCESSION NO
Arlington, VA 22217-5000				

DTIC
ELECTE
MAR 24 1993
S E D

11 TITLE (Include Security Classification)

Design of Interfaces in Metal Matrix Composites

12 PERSONAL AUTHOR(S)

Harris L. Marcus and Zwy Eliezer

13a TYPE OF REPORT	13b TIME COVERED	14 DATE OF REPORT (Year, Month, Day)	15 PAGE COUNT
Final Report	FROM 12/1/89 TO 11/30/92	February 15, 1993	

16 SUPPLEMENTARY NOTATION

COSATI CODES			18 SUBJECT TERMS (Continue on reverse if necessary and identify by block number)
FIELD	GROUP	SUB-GROUP	

19 ABSTRACT (Continue on reverse if necessary and identify by block number)

The main goal of this research was to optimize the interface properties in metal matrix composites by lattice matching the matrix and the dispersoids. Stable, coherent dispersoids can be achieved by mechanically alloying lattice-matched dispersoids into metal matrices and allowing some recrystallization or coarsening to occur, or by internal nitridization or carburization of homogeneous alloys. A model system that has a high probability of forming coherent interfaces is ZrN in Nb. For comparison purposed the relatively poorly matched systems TiN in Nb and TiN in Cu were also studies. The matrix/dispersoid orientation relationship in the Nb/ZrN system has been found to be $[011]_{Nb,Zr} \parallel [001]_{ZrN}$. In the Nb/TiN system, the presence of an orientation relationship after extensive nitriding could not be detected. In the Cu/TiN system only external nitridation occurred when bulk Cu-Ti alloys were employed. However uniformly distributed nanosized TiN dispersoids were obtained when alloyed Cu-Ti powders were nitrided and subsequently mechanically alloyed.

| 20 DISTRIBUTION / AVAILABILITY OF ABSTRACT	21 ABSTRACT SECURITY CLASSIFICATION
☒ UNCLASSIFIED/UNLIMITED ☐ SAME AS RPT ☐ DTIC USERS	Unrestricted
22a NAME OF RESPONSIBLE INDIVIDUAL S. Fishman	22b TELEPHONE (Include Area Code) (703) 696-0285	22c OFFICE SYMBOL

Form 1473, JUN 86   Previous editions are obsolete.   SECURITY CLASSIFICATION OF THIS PAGE

93 2 26 063

S/N 0102-LF-014-6603

DISCLAIMER NOTICE

DEFENSE TECHNICAL INFORMATION CENTER
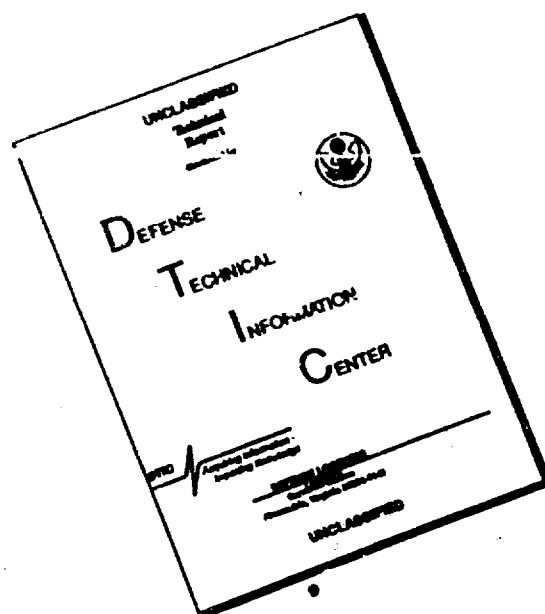
THIS DOCUMENT IS BEST QUALITY AVAILABLE. THE COPY FURNISHED TO DTIC CONTAINED A SIGNIFICANT NUMBER OF PAGES WHICH DO NOT REPRODUCE LEGIBLY.

Design of Interfaces in Metal Matrix Composites

Introduction

The main goal of this research is to optimize the interface properties in metal matrix composites by lattice matching the matrix and the dispersoids. An optimized interface should have excellent thermal stability, high strength, and an absence of brittleness. Good thermal stability is achieved by choosing phases that are in equilibrium with each other, interfaces with low surface energy and limited solubility to limit diffusion. High strength requires strong bonding across the interface. Absence of brittleness requires a larger extent of metallic bonding. Stable, coherent dispersoids can be achieved by mechanically alloying lattice-matched dispersoids into metal matrices and allowing some recrystallization or coarsening to occur, or by internal nitridization or carburization of homogeneous alloys. A model system that has a high probability of forming coherent interfaces is ZrN in Nb. For comparison purposes the relatively poorly matched systems TiN in Nb and TiN in Cu were also being studied. Other research areas that were investigated include processing approaches to create particulate composites These include high-energy high-rate processing and Selective Laser Reactive Sintering. The other approach is one in the new general area of Solid Freeform Fabrication approaches. A limited effort was done on evaluating the influence of residual stresses on the impact properties of graphite/aluminum matrix composites.

A brief discussion of the synthesis, processing, and characterization of the above mentioned systems is presented in the following paragraphs, with details in the attached appendices which are from submitted and published articles.

Accesion For		
NTIS CRA&I		X
DTIC TAB		☐
Unannounced		☐
Justification		
By		
Distribution /		
Availability Codes		
Dist	Avail and / or Special	
A-1		

1.   Nitridation of niobium alloys: interface effects

In this study metal matrix composites were fabricated by nitridation of solute-rich Nb-Ti and Nb-Zr alloys to form large volumes of nitrides. Studies of the kinetics of nitride formation and of the nature of the matrix-nitride interface were carried out. Nb-47.%Ti and Nb-47wt%Zr alloys were nitrided for different times and temperatures to nitride preferentially the solute phases into Ti- and Zr- rich nitrides. X-ray diffraction analysis confirmed the formation of the nitrides in the Nb solid solution matrix, and microhardness measurements explicitly indicated the hardening effect to be due to the formation of the nitrides. Orientation relationships were obtained between the matrix and the nitrides, but the habit planes were not defined. See appendix A for details.

2.   Attrition and Vibratory Milling of Cu-TiN

Two separate experiments involving attrition and vibratory milling of Cu-3wt.%TiN and Cu-25wt.%TiN respectively, were conducted. The results showed that a layered morphology occurred in the attrition milled specimen, but not in the vibratory milled sample. Massive agglomeration was observed in the attrition milled powder resulting in particles sizes larger that the starting powder sizes. In the vibratory milled case, excellent powder particle refinement occurred and nanosize copper and titanium nitride particles were observed under the TEM. In addition, consolidation of the vibratory milled powder did not cause much grain growth of the copper particles. The final result has been mostly attributed to the high volume fraction of TiN particles which may have inhibited large scale grain growth. See Appendix B for details

3. Internal Nitridation of Cu-Ti alloys.

Titanium nitride and Zirconium nitride possess relatively high electrical conductivity, high hardness and high melting point. Copper alloys dispersion hardened by TiN and/or ZrN may thus be a new promising class of alloys to be used in electronic packaging applications. Based on the insolubility and slow diffusion of N in Cu two routes for the formation of TiN in Cu alloys were studied.

(i) Surface nitridation of bulk Cu-Ti alloys which give a conductive mechanically hard surface.

(ii) Surface nitridation of fine Cu-Ti powders, followed by mechanical alloying to effectively break-up the TiN surface layers on the powder particles, and their solid state consolidation. This approach has resulted in a Cu-alloy strengthened by finely dispersed TiN particles and one that seems to hold its strength to high temperature. See Appendix C for details.

4. Processing of Metal Matrix Composites

The use of powder constituents in the processing and fabrication of metal matrix composites provides diverse and flexible routes for assembly of materials at the microscopic level. In the research that we describe here, the metal matrices were copper and tungsten. The dispersed phases were graphitic carbon and boron carbide. Most of the processing was performed with the constituents in the solid state . In the high energy high rate processing, energetic high-current pulses are directly applied to a powder mass to provide pulsed Joule heating. Heating rates of 1000 K/s to 10,000 K/s are achieved. When heat and pressure are simultaneously applied, rapid densification can occur. A homopolar pulse generator with 1 MA current capability has been used as a high-current source. The investigation of binderless

copper-graphite powder composites yielded materials with high densities, hardnesses and electrical conductivities. These materials have shown superior performance in terms of their high temperature capability and wear resistance in high-current, high-speed, electrotribological evaluation. The tungsten-based composite system offers a metallurgical cornucopia of phases including W, W_2C, FeWB, W_2B, Fe_3C, Fe_6W_6C, Ni_4B_3, and Fe_7W_6. These are obtained by reactions in the multicomponent system: W, Ni, Fe B, C. Some of these phases have large heats of formation and the consolidation proceeds by exothermic heating under pressure. The processing science based on these approaches has a common focus the understanding of the influence of basic processing parameters - time, temperature, and pressure - on the microstructure and properties of these composites. Details are provided in Appendix D.

5.   Development of a Selective Laser Reaction Sintering Workstation

A Selective Laser Reaction Sintering workstation has been developed at The University of Texas. The workstation allows the study of solid freeform fabrication of reaction sintered materials on a research scale. This technique has been applied to a variety of materials systems including a multilayer Cu-TiN rectangular solid. See Appendix E for details.

6.   Residual stress effect on impact properties of Gr/Al metal matrix composite

The effects of residual stress on the impact properties of the unidirectionally reinforced P 100 Gr/6061 Al metal matrix composites with different thermal histories have been investigated using an instrumented impact test method and scanning electron microscopy. The cantilever impact generally causes tensile failure at the notch and compressive loading on the opposite side of the specimen. The specimens with yield tensile matrix residual stresses have planar fracture

surfaces and low impact energy due to the contribution of tensile residual stress. The specimens with small residual stresses have moderate impact energy because debonding between fiber and matrix or fiber/matrix separation also serves as an additional mechanism for energy absorption. The specimens with higher compressive matrix residual stresses have the largest maximum load of all the specimens with the same matrix treatment. The specimen with matrix compressive yield residual stress has the maximum impact energy owing to a stepwise fracture surface. It can be concluded that good impact properties of composite materials can be obtained by choosing a suitable thermal history to modify the deleterious tensile matrix residual stress. For details of this research see Appendix F.

Nitridation of niobium alloys: interface effects

Michael Schmerling. S. Ponnekanti. S. T. Mear. A. Yeoh, Feng Chi. M. E. Fine. Z. Eliezer and H. L. Marcus

Center for Materials Science, The University of Texas at Austin. Austin. TX 78712 (USA)

Abstract

In this study metal matrix composites were fabricated by nitridation of solute-rich Nb-Ti and Nb-Zr alloys to form large volumes of nitrides. Studies of the kinetics of nitride formation and of the nature of the matrix-nitride interface were carried out. Nb-47wt.%Ti and Nb-47wt.%Zr alloys were nitrided for different times and temperatures to nitride preferentially the solute phases into Ti- and Zr-rich nitrides. X-ray diffraction analysis confirmed the formation of the nitrides in the Nb solid solution matrix, and microhardness measurements explicitly indicated the hardening effect to be due to the formation of the nitrides. Orientation relationships were obtained between the matrix and the nitrides, but the habit planes were not defined.

1. Introduction

Dispersion hardening is a common approach to strengthening metal alloys. Nitrides are often the dispersoid used. In many systems they show a lattice correspondence and low energy interface (habit) plane which causes a coherent particle strengthening mechanism to occur [1]. This investigation examines the results when higher concentrations of nitride formers are used. The intention was to form a metal matrix composite (MMC) with a ceramic high strength phase. An MMC benefits greatly from having a controlled strength interface between the components. It would be best to have low energy interfaces to achieve this strength and to establish metallurgical stability. Internal nitridation creates these interfaces *in situ* where they will tend to approach the lowest local energy state. The research presented here probed for the existence of these preferred low energy interfaces in several niobium alloys.

Niobium is an attractive major element for a class of high temperature alloys because of its relatively higher melting temperature 2467 °C and comparable density 8.6 g cm⁻³ to Ni (1453 °C and 8.9 g cm⁻³). While the Ni base superalloys may be made by conventional metallurgical processing. *i.e.* melting and heat treatment with or without mechanical deformation, no good precipitation hardening Nb-based system has been found. Nitrides of Zr and Ti have been formed in Mo by internal nitridation [2] and HfN has been similarly formed in W. W-Re and W-Re-Nb alloys [3]. Orientation relationships between crystal lattices and well defined habit planes were seen for the nitride precipitates in low concentration Ti and Zr in Mo alloys [1].

The same orientation relationships were seen in the present work using Nb (with presumably the same initial habit planes) owing to the similar atomic mismatches along $[100]_{B1} \| [110]_{bcc}$ directions and was part of the motivation for choosing these systems. It thus seemed possible to develop a class of Nb alloys with good mechanical properties by internal chemical reaction using easily diffused compound formers such as C and N.

For the internal chemical reaction to be successful a nitride or carbide of the solute in an Nb solid solution must have a substantially lower free energy of formation than that of Nb at the reaction and application temperatures. In addition, the diffusion rate of C or N in Nb must be more rapid than diffusion of the solute to the surface of Nb. If the latter is not true, a scale rather than an internal carbide or nitride will form.

For this study the formation of TiN and ZrN in a solute-rich Nb-Ti or Nb-Zr matrix by internal nitridation was considered. TiN and ZrN have substantially lower standard free energies of formation than NbN. At 1200 °C the standard free energy of formation is −48 kcal mol⁻¹ for NbN. −94 kcal mol⁻¹ for TiN. and −108 kcal mol⁻¹ for ZrN [4].

2. Experimental procedure

In the work presented here alloys of wrought Nb-47wt.%Ti 63.2 at.% Ti and arc-melted Nb-47wt.%Zr 47.5 at.% Zr were used for nitridation experiments. The Nb-47wt.%Ti is b.c.c. at all temperatures [5] and the Nb-47wt.%Zr is b.c.c. above approximately 950 °C. All the nitridation experiments were

performed in the single phase field. Below 950–610 °C there is a miscibility gap and a eutectoid reaction at 610 °C for Nb–Zr [6]. Samples were cut from the alloy materials and their surfaces ground to remove the oxide scale present. and then cleaned ultrasonically in acetone prior to nitridation.

Homogeneity of the alloys was established using energy-dispersive spectrometry (EDS) and X-ray diffraction (XRD) techniques. EDS was used by taking a composition profile over a 3×3 square point grid. XRD was performed on a polished surface of the alloy samples.

Initially, samples were nitrided by placing them in a DTA furnace at combinations of several times (2, 4, 8, 24 h) and temperatures (1080–1300 °C) in a pure nitrogen gas environment. To flush the system of detrimental oxygen or other possible contaminants, nitrogen gas was passed over the sample throughout the cycle. However, the residual oxygen and the strong oxide-forming nature of the Nb alloys resulted in oxide formation on the sample surface.

In order to control the oxidation during nitridation, an alumina tube furnace was constructed. Residual oxygen in the system was gettered through the use of titanium powder. The experimental set-up for the furnace is shown in Fig. 1. The samples, immersed in Ti powder, were put in an alumina boat. The system was evacuated and then flushed with ultrahigh purity (99.999%) nitrogen for 2 h prior to the start of each experiment.

Samples were characterized using optical microscopy, Vickers microhardness, Auger electron spectroscopy (AES), scanning electron microscopy (SEM), XRD, EDS, and transmission electron microscopy (TEM).

In the Nb–Zr system X-ray samples (1 cm × 1 cm × 0.3 cm), metallographic samples ($0.2 \times 0.2 \times 0.7$ cm^3), and TEM samples (1 cm × 1 cm × 15 mil thick) were simultaneously nitrided in the tube furnace at 1200 °C for 24 h. The sample to Ti getter volume ratio used for this alloy system was 0.7.
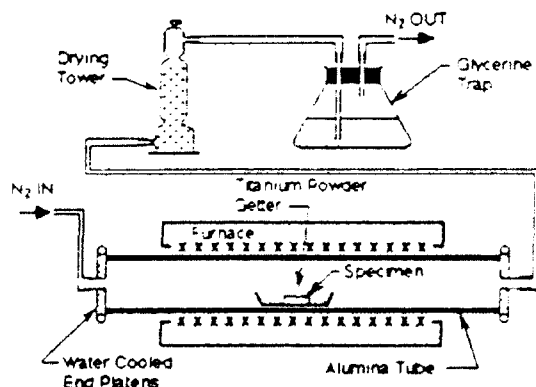
The nitrided Nb–Zr X-ray diffraction patterns were taken with an Si standard. This was repeated after grinding off an approximately 50 mm layer each time to determine the extent and the nitride phase formed. The metallographic samples of Nb–Zr–N were cut and mounted to observe the true cross-section under the microscope. An etchant of the composition 50 ml H$_2$O, 25 ml HNO$_3$ and 5 mml HF, was used to etch preferentially the Nb. A microhardness test was performed on the cross-section (unetched) using Vickers hardness indentation with a 200 g load. The TEM sample was ground to 2 mil before being argon ion beam milled (0.75 mA, 5 kV) from both sides until a small hole appeared (approximately 14 h).

In the Nb–Ti–N system samples for optical microscopy, microhardness, AES and SEM analysis, were prepared by cross-sectioning to a final polish with 0.5 μm alumina slurry. The SEM samples were sputter-coated with a layer of Au–Pd. SEM analysis was performed on both unetched samples and samples in which the Nb–Ti matrix surrounding the TiN features had been preferentially etched away using an etchant of one part hydrofluoric acid and three parts nitric acid. After nitriding, TEM samples were prepared as described previously. For both alloys AES was used to determine the approximate chemistry of the nitride.

3. Results

EDS and SEM confirmed the homogeneity of the samples. The X-ray diffraction patterns taken off the polished surfaces showed only the presence of a solid solution of Zr and Nb in the Nb–Zr system for samples quenched from the single phase field and a solid solution of Nb and Ti in the Nb–Ti system, with no indication that the alloys contained any other phases.

In the Nb–Zr–N system the XRD pattern on the surface of the nitrided sample showed the presence of ZrN, Ti (from the getter), and an oxynitride of the Nb solid solution. After grinding off a layer of 100 μm the pattern showed the presence of an Nb solid solution and ZrN. Further grinding to 200 μm, the pattern showed the base Nb–Zr solid solution, indicating that the nitrided layer was about 200 μm thick. Figure 2 shows the XRD patterns taken after periodic grinding.

Microhardness tests, performed angularly on the cross-section, showed a twofold increase in the Vickers hardness number from the inner material to the nitrided crust. A schematic drawing of the true cross-section of the sample along with the microhardness data is shown in Fig. 3.

TEM analysis of the sample showed the presence of ZrN in an Nb–Zr solid solution matrix. Figure 4 illustrates the morphology. Diffraction patterns at the inter-
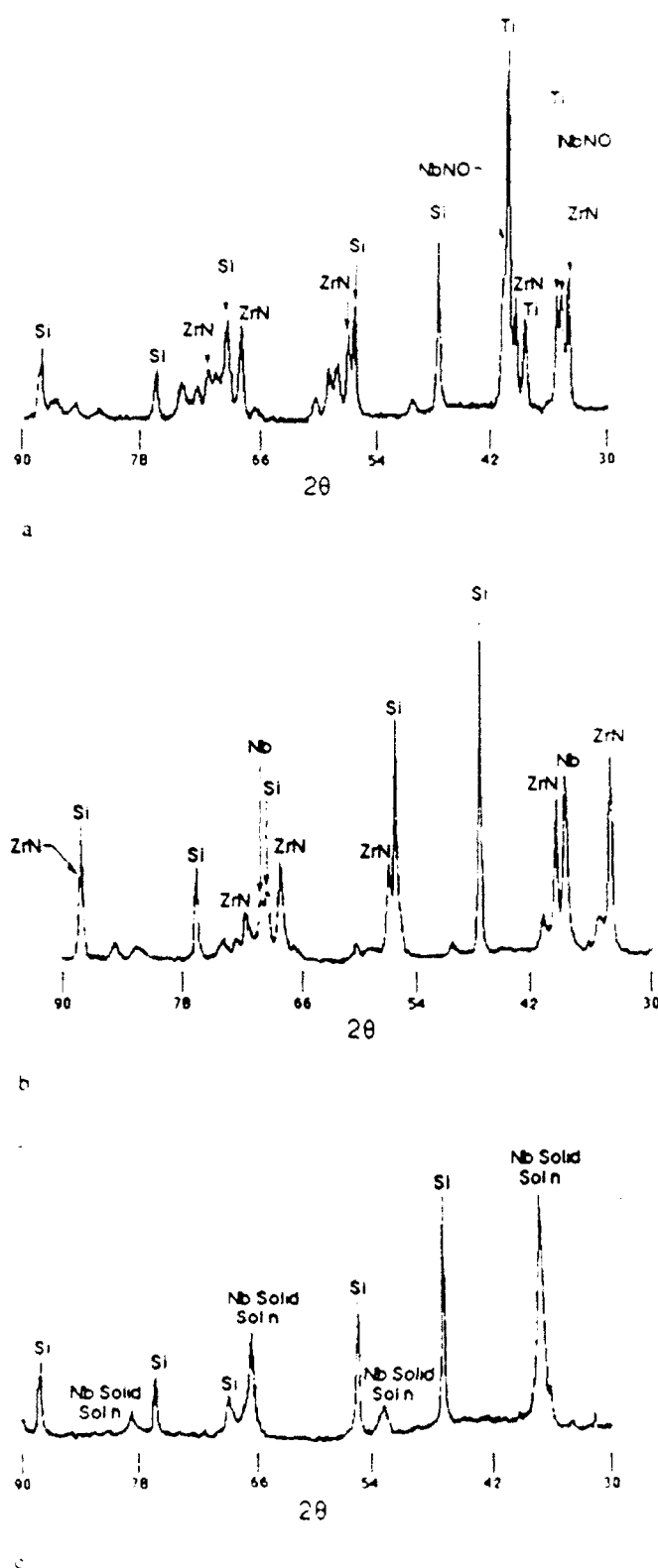
faces showed that there is an orientation relationship between the Nb-rich solid solution and ZrN volumes in most areas of the thin foil TEM sample. Figure 5 shows an interface and the corresponding diffraction pattern. The diffraction patterns showed the orientation relationship to be $[001]_{Nb-Zr} \| [001]_{ZrN}$. This is equivalent to the $[001]_{Nb-Zr} \| [011]_{ZrN}$ for $[001]_{bcc} \| [001]_{fcc}$. A simple lattice matching model shows this to be a low energy match due to the small, approximately 2%, mismatch. The boundaries between the solid solution and ZrN did not appear to be the simple $\{001\}_{bcc} \| \{001\}_{fcc}$ plane expected for small precipitates, indicating that the planar low energy interface was probably only present at an early point in the ZrN growth. This early growth dictated the orientation relationship but as growth continued other factors influenced the exact phase boundary morphology.

A sample of Nb–Ti which was nitrided in the DTA for 24 h at 1200 °C was cross-sectioned and then mechanically polished. AES was performed on this sample. From a comparison of the Auger spectrum of the sample with the spectrum from pure (99.9%) TiN powder, TiN was determined to be present in the sample. However, the spectrum showed that a large amount of oxygen contaminant was also present in the surface layer. XRD determined that the surface oxide present in the sample was $Nb_2TiO_?$.

Figure 6 is a micrograph of the EDS line scans for Nb and Ti on a polished sample which was nitrided for 4 h at 1080 °C. The white line across the sample is the location across the sample for which the scan was performed. From the line scan, there appears to be an excess concentration of Ti at the grain boundaries. These regions appear to be zones where nitrogen has reacted with the matrix material. Thus both bulk diffusion of nitrogen and diffusion of nitrogen along grain boundaries play an important role. As the nitridation temperature is increased to 1200 °C and then 1300 °C and the reaction time increased from 4 to 24 h the progression of the reaction front can be followed until complete reaction of the base material with the nitrogen has occurred throughout the specimen.
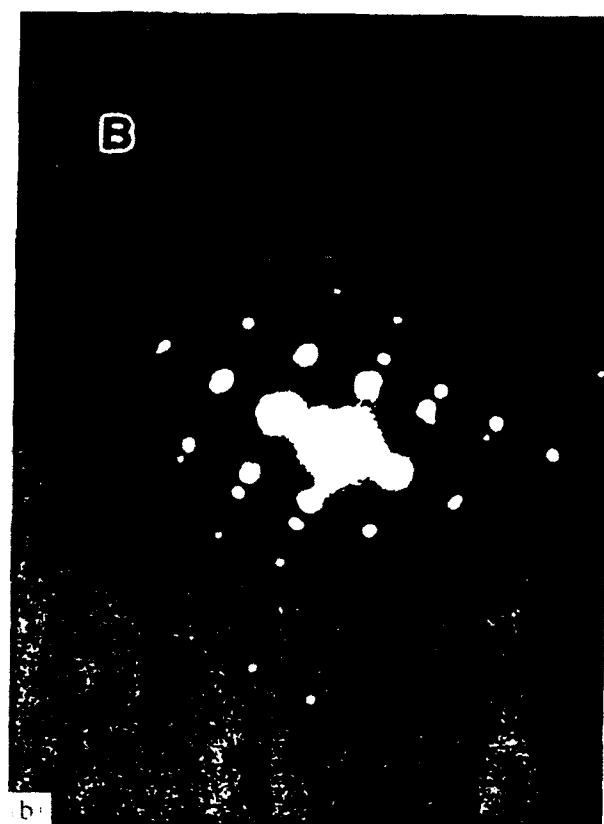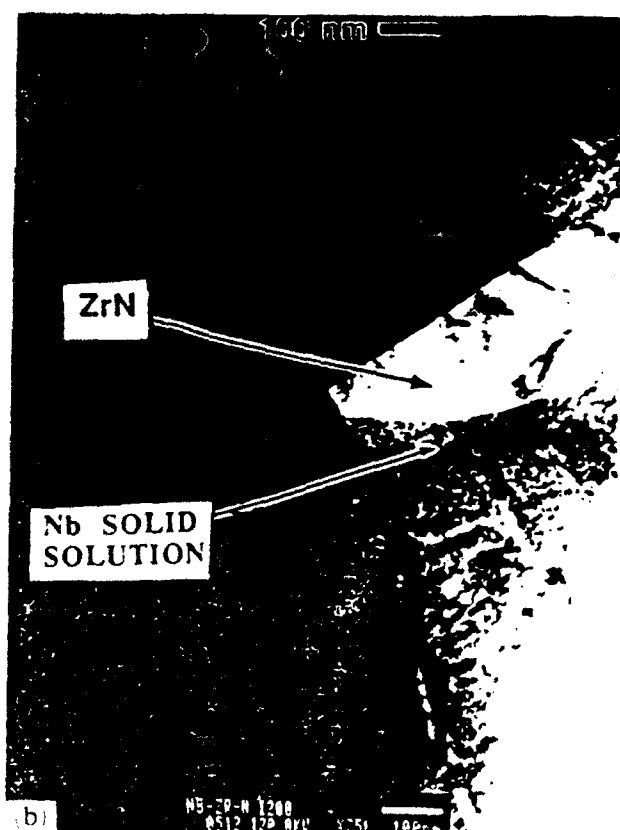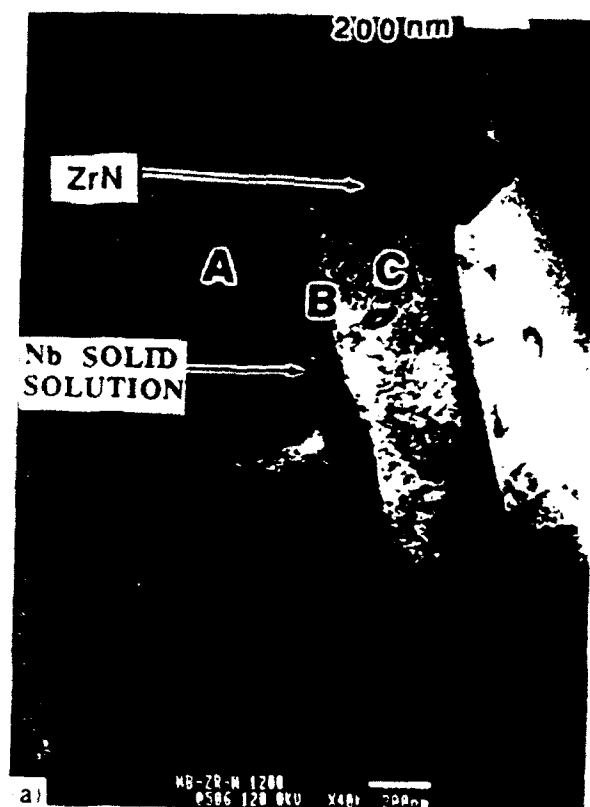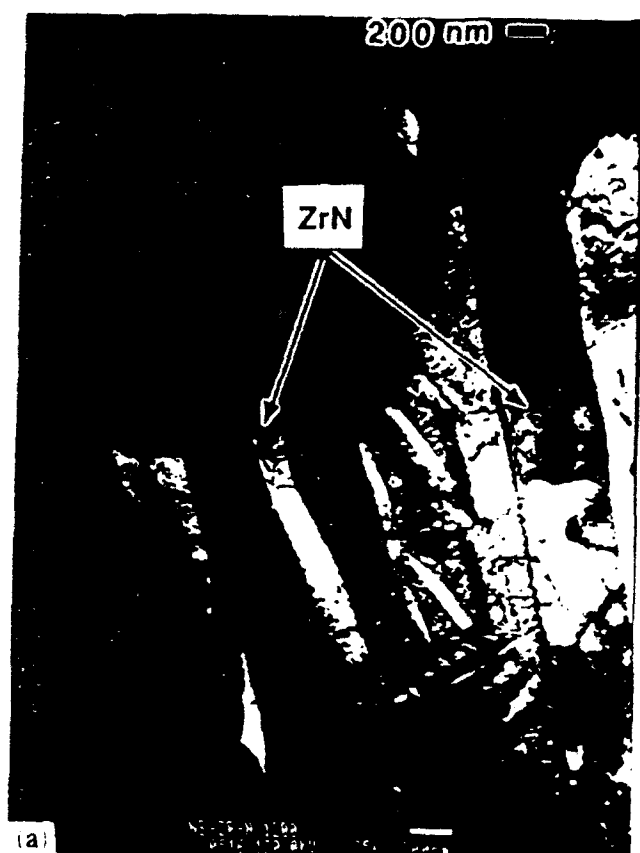
Fig. 4. (a) TEM image showing ZrN volumes in an Nb solid solution matrix; (b) TEM image showing ZrN volumes in an Nb solid solution matrix in another section of the sample.

Fig. 5. (a) TEM image of the interface between ZrN and Nb solid solution matrix; (b) diffraction pattern at the interface with $[110]_{Nb-Zr} \| [100]_{ZrN}$.
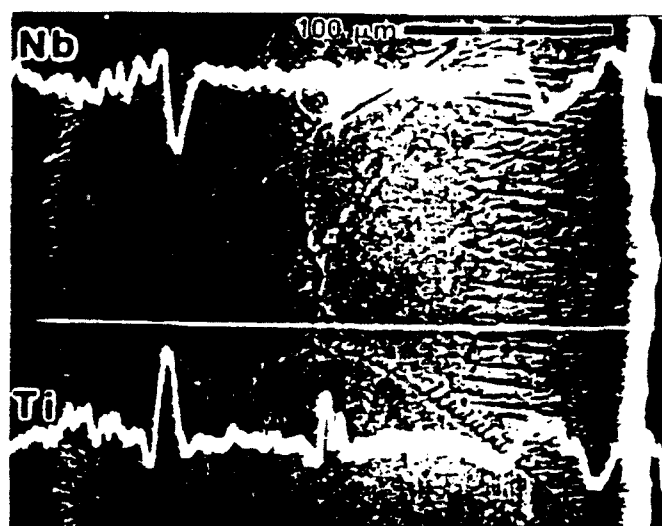
Fig. 6. EDS line scan of Nb-47wt.%Ti nitrided for 4 h at 1080 °C showing concentration of Ti at grain boundaries.

Figure 7 shows a sample nitrided for 4 h at 1200 °C which has had the Nb-Ti matrix etched away to show "TiN rods". EDS shows these rods to be rich in Ti. The solid solution chemistry is approximately $Nb_{0.2}Ti_{0.8}N$. The "rods" were confirmed to be solid solution TiN from the TEM diffraction patterns. Figure 8 shows a TEM image of a sample nitrided for 4 h at 1200 °C. The rod-like structures in this figure correspond in size and shape to those in Fig. 7. The orientation relationships between the Nb-Ti matrix and the TiN were determined to be:

$$[100]_{Nb-Ti} \| [110]_{TiN}$$

$$[113]_{Nb-Ti} \| [112]_{TiN}$$

These relationships are consistent with those found for TiN in Mo by Ryan and Martin [1] but not with that predicted by simple matching of the B1 (NaCl) TiN crystal structure with the b.c.c. Nb-Ti solid solution crystal structure along (100) planes of both where $[100]_{bcc} \| [110]_{B1}$ and $[110]_{bcc} \| [100]_{B1}$. This orientation shows a mismatch of approximately 9% along a [110] direction. The orientation relationship is not as simple as that found for Nb-Zr solid solution-ZrN system where the mismatch along the [110]_{bcc} is about 2%. It was suspected that early in the growth the habit plane was the (310)_{Nb-Ti} (311)_{TiN} by analogy with the Mo-TiN system.

AES was performed on a mechanically polished sample which had been nitrided for 24 h at 1200 °C. Again, TiN was determined to be present using AES. A very thin surface oxide was also observed. Only a small amount (less than 5 min) of inert ion sputtering was required to reduce the AES oxide signal to a negligible amount. SEM images of samples prepared in the tube furnace, both unetched and etched, show the reaction
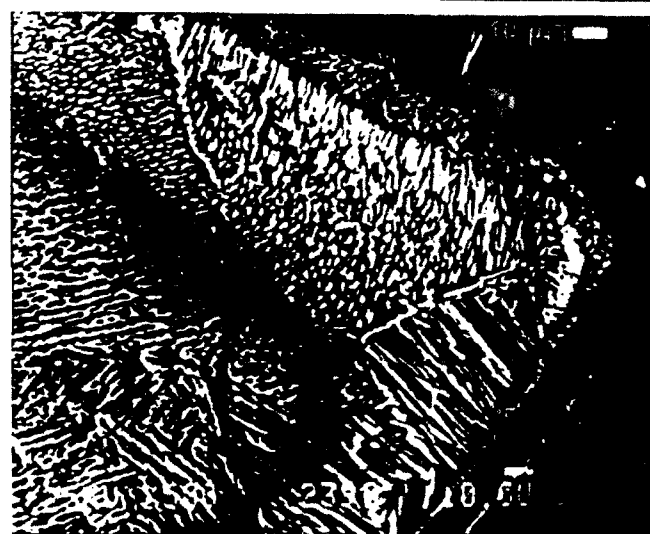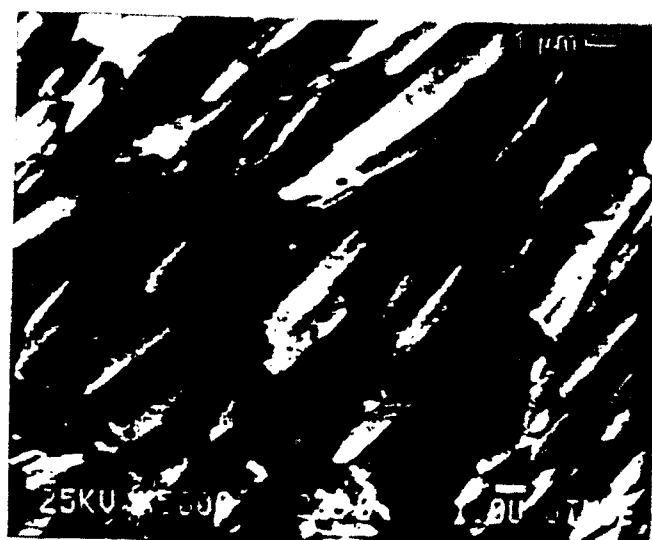

Fig. 7. SEM images of Nb-47wt.%Ti nitrided for 4 h at 1200 °C which has had the matrix etched away to show "TiN rods".

front of the nitrogen, grain boundary diffusion of the nitrogen, and the rod-like TiN features.

TEM analysis could not confirm the continued presence of an orientation relationship after extensive nitriding (24 h at 1200 °C). Regions of TiN were found surrounded by Nb-rich solid solution. While regions which contained some elongated rods of TiN were found, the bulk of the rods spheroidized to equiaxed grains of TiN solid solution.

4. Discussion

After nucleation and growth of small oriented nitride particles, nitrogen is continuously supplied through the solid solution-nitride phases produced at the free surface and the growth continues by a cellular growth mechanism. Figure 9 shows a schematic dia-
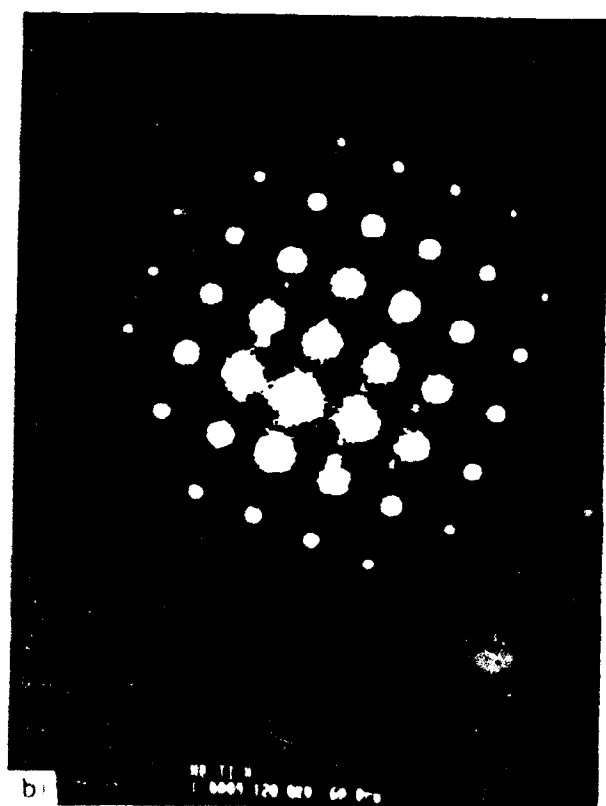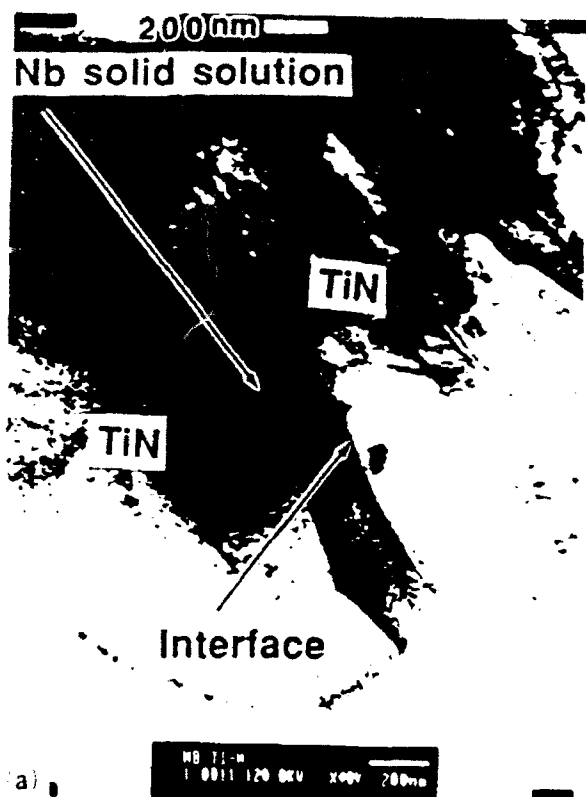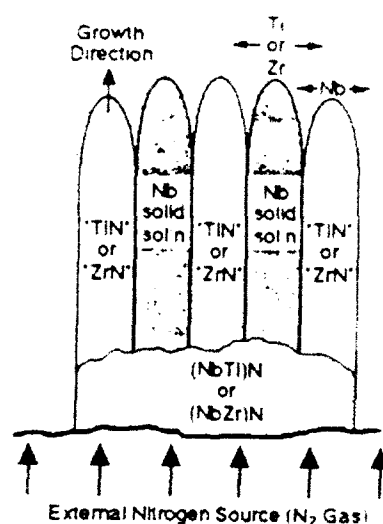
(a)

NITRIDE GROWTH MECHANISM

Fig 9. Schematic diagram of growth of TiN or ZrN in Nb solid solution matrix.
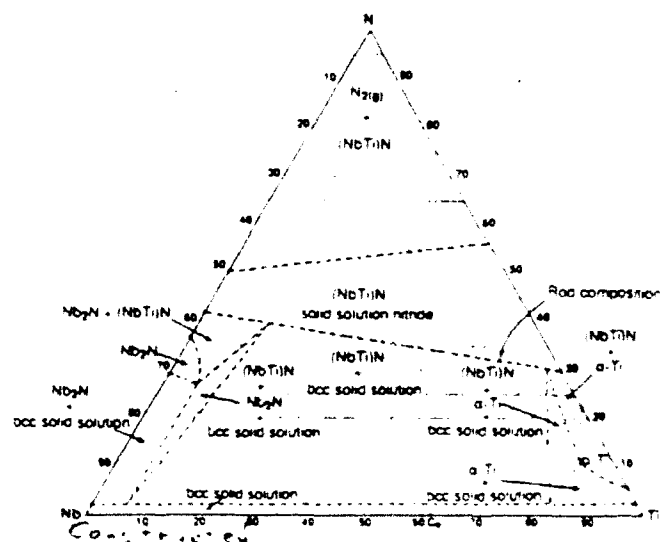

Fig. 10. Isothermal section 1200 °C of Nb-Ti-N ternary atomic per cent, showing TiN rod composition. ● data points from existing binary phase diagrams

Fig. 8. (a) TEM image of the interface between TiN rod and Nb solid solution matrix; (b) diffraction pattern at the interface with $[100]_{Nb-Ti} \parallel [110]_{TiN}$.

gram for the cellular nitride TiN or ZrN growth process. Nitrogen diffuses in the bulk and along grain boundaries. The Ti or Zr reacts with the nitrogen to form the nitrides, leaving the Nb matrix with a lower content of solute. Continued nitriding after forming this MMC consisting of a ceramic nitride phase surrounded by an Nb-Ti or Nb-Zr solution matrix leads to spheroidization and formation of a solid solution nitride. Figure 10 shows a 1200 °C isothermal cut from the ternary phase diagram constructed from data from

this study, the Nb-Ti, Nb-N, and Ti-N binaries, as well as from literature data [7]. The phases shown are consistent with those present in the internally nitrided samples.

Cellular growth in the Nb-Ti system is indicated by the TiN rods which are formed in the above sample nitrided for 4 h at 1200 °C but apparently change morphology with continued nitriding time *e.g.* the 24 h, 1200 °C sample). The conditions controlling the lattice correspondence between the phases seem to change with growth of the nitride, probably owing to the formation of the solid solution nitride. The lattice correspondence seen in Mo-based alloy dispersoids is still seen during cellular growth in Nb-Ti-N and Nb-Zr-N but there is evidence that it is lost with increasing nitridation in the Nb-Ti-N system. Even when a lattice correspondence exists in these samples, the interface is no longer controlled only by the energy conditions which dictated the low energy plane when it was initially nucleated. The curved interfaces observed in all samples investigated were no longer simple habit planes at the observed magnifications.

5. Summary

Internal nitridation of an Nb-47wt.%Ti and an Nb-47wt.%Zr alloy was performed in a pure nitrogen environment at 1200 °C. The lower free energy nitrides, TiN and ZrN, formed in preference to NbN in the respective solid solution systems. Initially, an orientation relationship between the Nb solid solution and the nitrides was present in both systems. However, in the Nb-Ti system the relationship was lost after increased nitridation times owing to spheroidization of the solid solution TiN phase. A schematic for this growth process was defined. An isothermal section of Nb-Ti-N ternary at 1200 °C was constructed from the results of these experiments, from the binary phase diagrams, and from literature data.

Acknowledgments

References

1 N. E. Ryan and J. W. Martin, in F. Benesovsky ed., *High Temperature Materials*, Metallwerk Plansee, Reutte, 1968, pp. 182-207.
2 A. K. Mukjenee and J. W. Martin, *J. Less-Common Met.*, 2 (1960) 392; 3 (1961) 216.
3 D. J. Iden and L. Himmel, *Acta Metall.*, 17 (1969) 1483.
4 T. Rosenqvist, *Thermochemical Data for Metallurgists*, Tapir Forlag, 1970.
5 J. L. Murray (ed.), *Phase Diagrams of Binary Titanium Alloys*, ASM International, Metals Park, OH, 1987.
6 M. Hansen and K. Anderko, *Constitution of Binary Alloys*, Metallurgy and Metallurgical Engineering Series, 1958.
7 O. M. Barbash and A. K. Shurin, *Metallofizika*, Inst. Metallofiz., Kiev, 1978.

2. Muknergee

ATTRITION AND VIBRATORY MILLING OF Cu-TiN

A. YEOH, M. SCHMERLING, H. L. MARCUS and Z. ELIEZER

Center for Materials Science and Engineering

The University of Texas at Austin

Austin, Texas 78712

Mechanical alloying or high-energy ball milling is a solid-state powder processing method first developed by J.S. Benjamin in the late 1960's [1]. In mechanical alloying, metal and/or ceramic powders are repeatedly fractured and welded resulting in individual alloyed powder particles. Typically, hard ceramic or metal balls are used as grinding media, hence the term ball milling. Commercially, mechanical alloying has been used for many applications including the manufacture of oxide dispersion strengthened superalloys [2], and more recently, the production of amorphous powders [3].

Generally, it is accepted that ball milling produces powder particles with a characteristic lamellar structure [4]. However, this study of Cu-TiN showed that the lamellar morphology was observed only in attrition milled powders and not in vibratory milled powders.

In the attrition milling experiment, a Szegvari^{TM} HD-01 attritor utilizing stainless steel parts was used. 200 grams of 3/16 inch diameter stainless steel balls were selected as the grinding media for 50 grams of Cu powder mixed with TiN powder to produce a Cu-3 wt.%TiN composition. The average starting Cu powder size was ~75 μm and the average starting TiN powder size was ~3 μm as depicted in Figure 1. After sealing the powders

1

and grinding media in the tank, the system was purged with argon for 2 hours before commencing the experiment. An argon flow rate of 0.8 L/min was maintained throughout the experiment. The actual experiment was conducted with a rotational speed of 600 rpm which corresponds to a calculated ball collision speed of approximately 2.5 m/s. It should be noted, however, that according to Courtney and Maurice [5] the average collision speed in the attrition mill may not exceed 0.5 m/s. Flowing tap water (~20°C) was used as a tank coolant throughout the 8 hour period of the run. At the end of the run the milled powder was allowed to cool under the same argon flow for 2 hours. The powder was then removed and stored in a vacuum desiccator for future analysis.

A Spex^{TM} 8000 Mixer/Mill with hardened steel components was used for the vibratory milling experiments. Three 1/2 inch diameter hardened steel balls with a combined mass of 25 grams were used as the grinding media for 10 grams of Cu-25 wt.%TiN powder mixture. Similar to the attrition milling experiment, the powders were manually mixed prior to placement within the grinding vial. The same starting powders were used but with a different weight ratio than during attrition milling. The vial was then capped in an argon atmosphere and was not opened again until the end of the 16 hour run. Due to the nature of the vibratory mill apparatus no tank coolant was used, but internal temperatures were expected to be higher due to collision speeds on the order of 17 m/s [5]. At the end of the experiment, the milled powder was left within the vial for 4 hours (to allow sufficient cooling) prior to removal and storage in a vacuum desiccator.

Before examining the milled powders, it was expected at this point that both powder specimens would yield intimately mixed powder particles with a lamellar morphology. The vibratory milled powders were expected to be much finer due to the reported efficacy of the vibratory milling process. Suryanarayana and Froes [6] have

2

claimed that 16 hours of milling in the vibratory mill is equivalent to 100 hours in the attrition mill.

The milled powders were characterized in loose form and in mounted and polished form in a scanning electron microscope. The loose specimens were prepared by placing a small amount of milled powder on an aluminum stage and sputter coating the sample with gold-palladium. Preparing the polished specimen involved mounting the loose powder in bakelite, manual grinding to 600 grit SiC paper, rough polishing with a 1 μm diamond paste, and finally fine polishing with a 0.05 μm Al_2O_3 slurry. In between each step the specimen was cleaned with ethanol in an ultrasonic cleaner. After fine polishing, both samples were etched for copper using an etchant consisting of 3 parts glacial CH_3CO_2H to 1 part HNO_3. Finally, the specimen was also sputter coated with gold-palladium for the SEM analysis.

SEM micrographs of the 8 hour attrition milled Cu-3 wt.%TiN powder is depicted in Figure 2. When compared to the starting copper powder, it was obvious that the milled powder particles were actually agglomerations of smaller particles. This observation was also made directly from the "layered" appearance of the milled powder particles. After polishing and etching for copper, the lamellar structure characteristic of mechanically alloyed powders became more evident. Closer inspection of Figure 2(b) reveals that the lamellae within the agglomerates consists of submicron folds. A well dispersed distribution of submicron titanium nitride particles between the copper folds can also be seen in this micrograph. Therefore, ball milling appears to have refined the titanium nitride particles. Submicron copper "folds" had also been concurrently formed, but agglomeration of these "folds" effectively negated copper particle refinement as it is the size of the individual/agglomerated powder particles that is important during subsequent

3

consolidation. Hence, attritor milling had effectively formed large dispersion strengthened powder particles.

Figure 3 is an SEM micrograph of the loose 16 hour vibratory milled Cu-25 wt.%TiN powder. Agglomeration can be observed throughout the powder specimen, hut these agglomerates comprised submicron copper and titanium nitride individual particles. Upon polishing and etching the powder specimen, no lamellar morphology was observed. Instead, a very good dispersion of fine TiN particles within a "smooth" copper matrix was observed as depicted in Figure 4. The powder specimen was consolidated via compaction and conventional sintering in H_2 (1000°C for 4 hours), then sectioned and thinned for transmission electron microscope (TEM) investigation. Figure 5 is a TEM micrograph showing the selected area diffraction (SAD) patterns from two adjacent regions. The ring pattern indicated that polycrystalline copper was present at this scale, which was extremely surprising considering that the specimen had been heat treated at a temperature conducive to accelerated grain growth of copper. A possible explanation for this occurrence is that the high content of TiN particles during milling could have functioned as minute grinding agents. Hence, the already effective refinement method via vibratory milling is further amplified by the presence of these small, hard particles. The milling process also disperses the small TiN particles (which are also refined to submicron dimensions) that inhibit grain growth of the copper, yielding a nanosize polycrystalline copper/titanium nitride composite.

As described, a lamellar morphology was observed in the attrition milled sample, but none was observed in the vibratory milled specimen. This is possibly an effect of the higher concentration of TiN powder in the latter experiment. However, ultrafine grains of copper remained after this powder specimen was compacted and sintered indicating a homogeneous distribution of TiN in Cu as opposed to a layered morphology. This

4

homogeneity in the 25 wt.%TiN specimen may also be due to the larger volume percentage of brittle phase surrounding the small copper particles which prevented large scale agglomeration.

In summary, two separate experiments involving attrition and vibratory milling of Cu-3 wt.%TiN and Cu-25 wt.%TiN respectively, were conducted. The results showed that a layered morphology occurred in the attrition milled specimen, but not in the vibratory milled sample. Massive agglomeration was observed in the attrition milled powder resulting in particle sizes larger than the starting powder sizes. In the vibratory milled case, excellent powder particle refinement occurred and nanosize copper and titanium nitride particles were observed under the TEM. In addition, consolidation of the vibratory milled powder did not cause much grain growth of the copper particles. The final result has been mostly attributed to the high volume fraction of TiN particles which may have inhibited large scale grain growth.
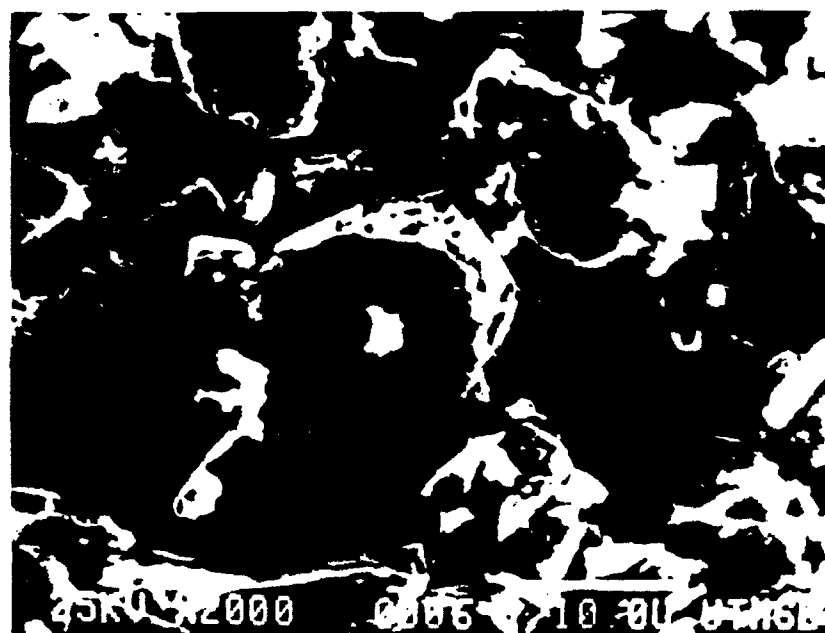
References

1. J. S. BENJAMIN, *Met. Trans.* 1 (1970) 2943.

2. J. R. RAIRDEN and E. M. HABESCH, *Thin Solid Films* 83 (1981) 353.

3. R. B. SCHWARTZ and C. C. KOCH, *Appl. Phys. Lett.* 49 (1986) 146.

4. M. J. FLEETWOOD, *Mat. Sci. Tech.* 2 (1986) 1176.

5. T. H. COURTNEY and D. R. MAURICE, *Met. Trans. A* 21 (1990) 283.

6. C. SURYANARAYANA and F. H. FROES, *J. Mat. Res.* 5 (1990) 1880.

Acknowledgements
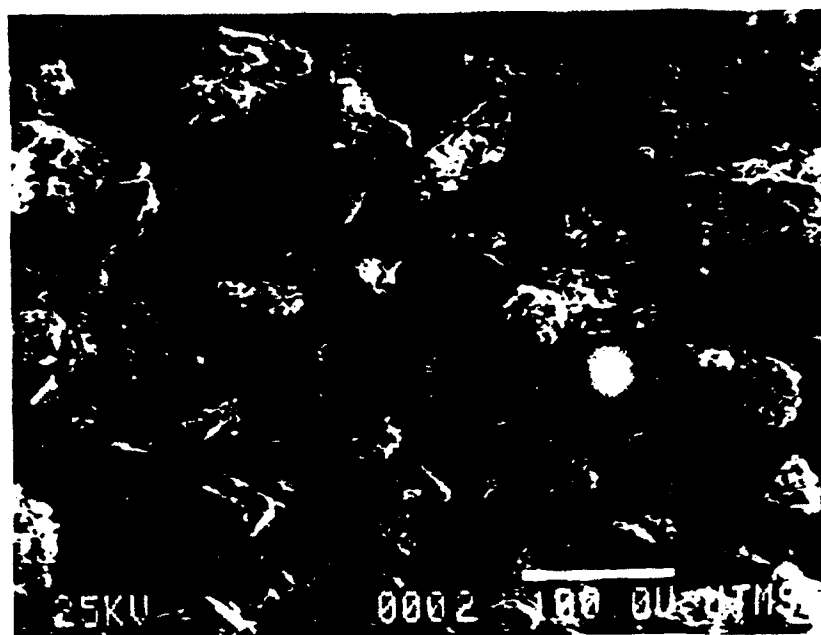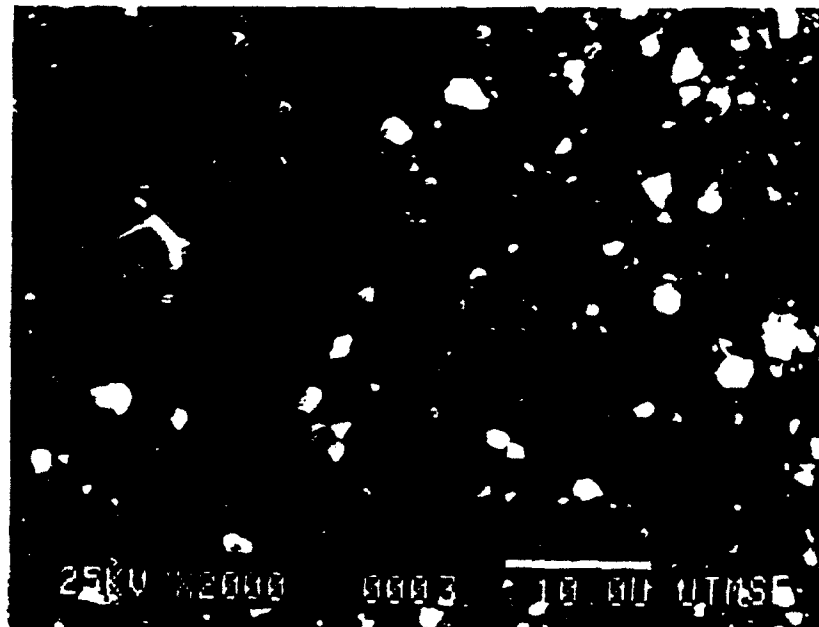
Figure 1 SEM micrographs of the (a) starting copper powder and (b) starting titanium nitride powder.

(a)

(b)

Figure 2 SEM micrograph of the (a) 8 hour attrition milled Cu-3 wt.%TiN powder (b) after polishing and etching for copper.

Figure 3 SEM micrograph of the 16 hour vibration milled Cu-25 wt.%TiN powder.

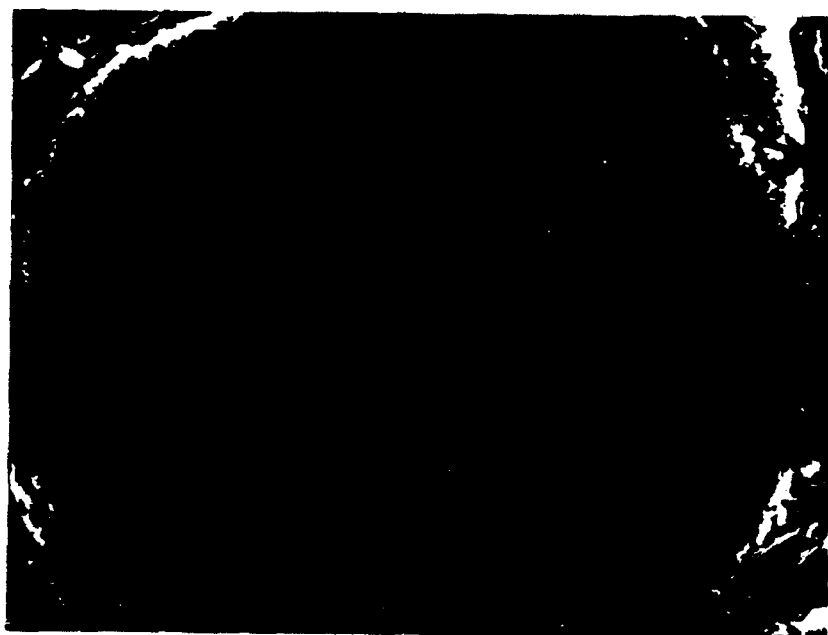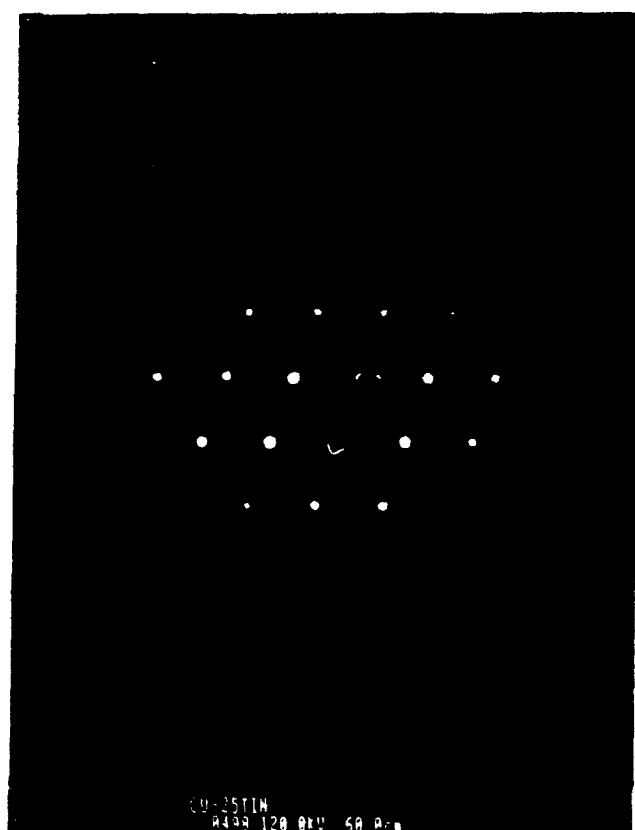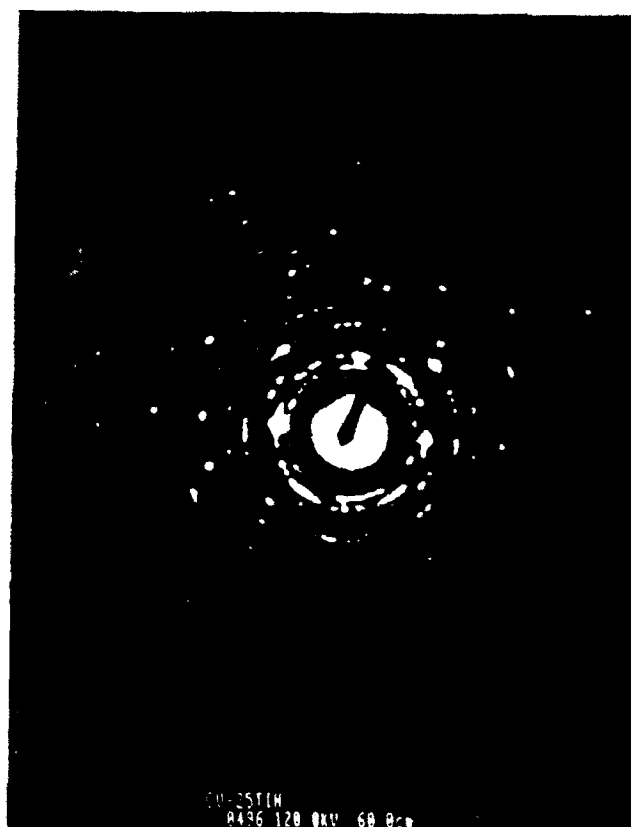**Figure 4** SEM micrograph of the 16 hour vibration milled Cu-25 wt.%TiN powder after polishing and etching for copper.

Figure 5 (a) TEM micrograph of 16 hour vibration milled Cu-25 wt.%TiN powder
after sintering with (b) the diffraction pattern from A - TiN_{110}, and
(c) the diffraction pattern from B - polycrystalline copper.

Copper alloys dispersion-strengthened by nitrides

Copper when dispersion strengthened by oxides (Al_2O_3, TiO_2, ZrO_2 and BeO), borides (TiB_2) and carbides (ZrC, TaC and NbC) offers a unique combination of high strength and hardness with excellent electrical conductivity. Such alloys are used for lead frames, spot welding electrodes, etc. The effectiveness oft the dispersed particles in the matrix strengthening and strength retention depends upon the particle size, interparticle spacing and chemical stability. Transition nitrides such as TiN and ZrN possess high electrical conductivity, high hardness and melting point. It is expected that a copper alloy dispersion hardened by TiN and ZrN would be extremely useful. However, little research has been done on these systems. The object of this investigation was to make TiN dispersion hardened copper alloys which possess high strength and high electrical conductivity at high temperatures.

The experimental procedure is shown in the following block diagram.

Cu-3wt%Ti mixture → Mechanical alloying → Alloyed Cu powder → External nitridation → TiN coated Cu powder → Mechanical alloying → Cu-TiN alloy

Mechanical alloying was performed with a Spex 8000 mixer/mill using hardened steel vial and grinding balls 12.7 mm in diameter. The milling process was interrupted periodically and a small amount of the powder was taken out from the vial in a glove bag filled with high purity nitrogen. After nitridation, the powder was finally mechanically alloyed for 10 hours. All external nitridation was carried at 800°C for 24 hours. The ball milled powder was characterized by X-ray diffraction (XRD) using Cu $K\alpha$ radiation. Scanning electron microscopy (SEM) was used for morphological examination. Auger electron spectra (AES) were obtained using 3 Kev electron beam while the sample was sputtered with Ar ion at $4*10^{-7}$ torr. Vickers microhardness values were determined for the consolidated and high temperature annealed samples using a load

of 200g. Carbon extraction replicas were employed to observe the TEM images of the dispersed nitride particles. Some TEM samples were also prepared by Ar ion beam thinning.

The powder mechanically alloyed for 57.6 ks was nitrided at 1073 K for 86.4 ks and became golden colored. A TiN layer formed on surfaces of powders as confirmed by X-Ray diffraction analysis (Fig. 1) and SEM microphotographs (Fig. 2). The nitrided powder was then spex-milled for 36 ks. It is interesting to note that almost theoretical density was obtained during the mechanical alloying process. The loose powders have changed into small agglomerates of various size, some as big as 6 mm in diameter. Few pores were observed under SEM examination (Fig. 3).

Fig 4 is the TEM image of the extracted dispersed TiN particles and the corresponding selected area diffraction pattern. It is clear that nanosized TiN particles were obtained by this *external nitridation method in combination with mechanical alloying.* Occasional particles of the nitride phase on the order of 1μm were seen. Selected area diffraction ring patterns indicate that these larger particles consist of many small TiN particles. These agglomerates were annealed at elevated temperature in vacuum and showed very high room temperature hardness values which were independent of annealing temperature below 1173 K as shown in Fig. 5.

At this stage, mechanical alloying in combination with external nitridation seems to be a very promising technique for the preparation of copper alloys dispersion-hardened with nitrides.

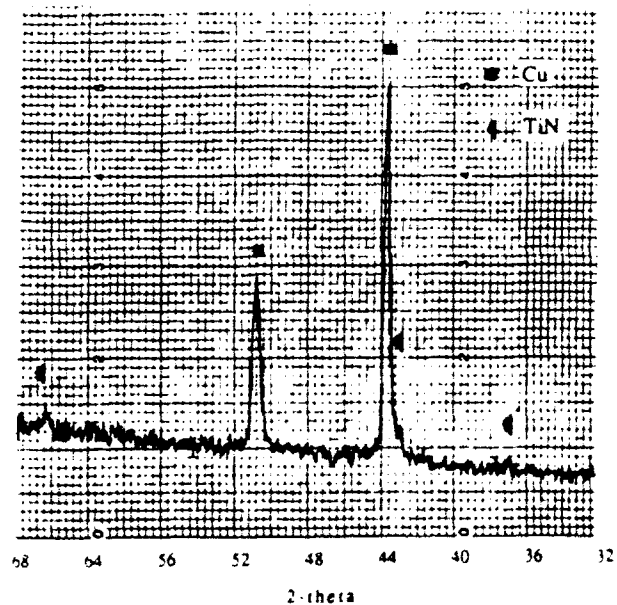Fig. 1 X-ray diffraction pattern for the sample
nitrided at 1073 K for 86.4 ks

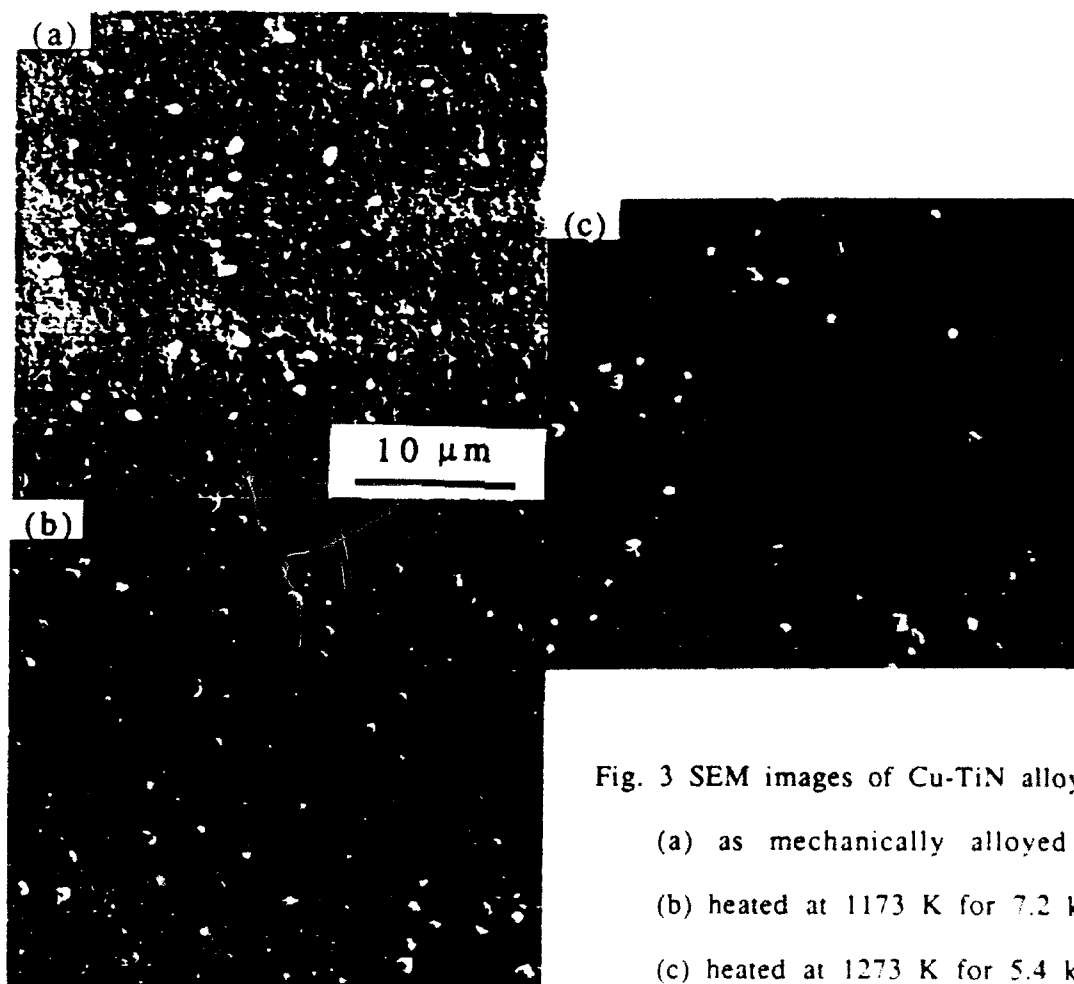Fig. 2 SEM image for the sample nitrided at 1073 K for 86.4 ks

10 μm

Fig. 3 SEM images of Cu-TiN alloys

(a) as mechanically alloyed

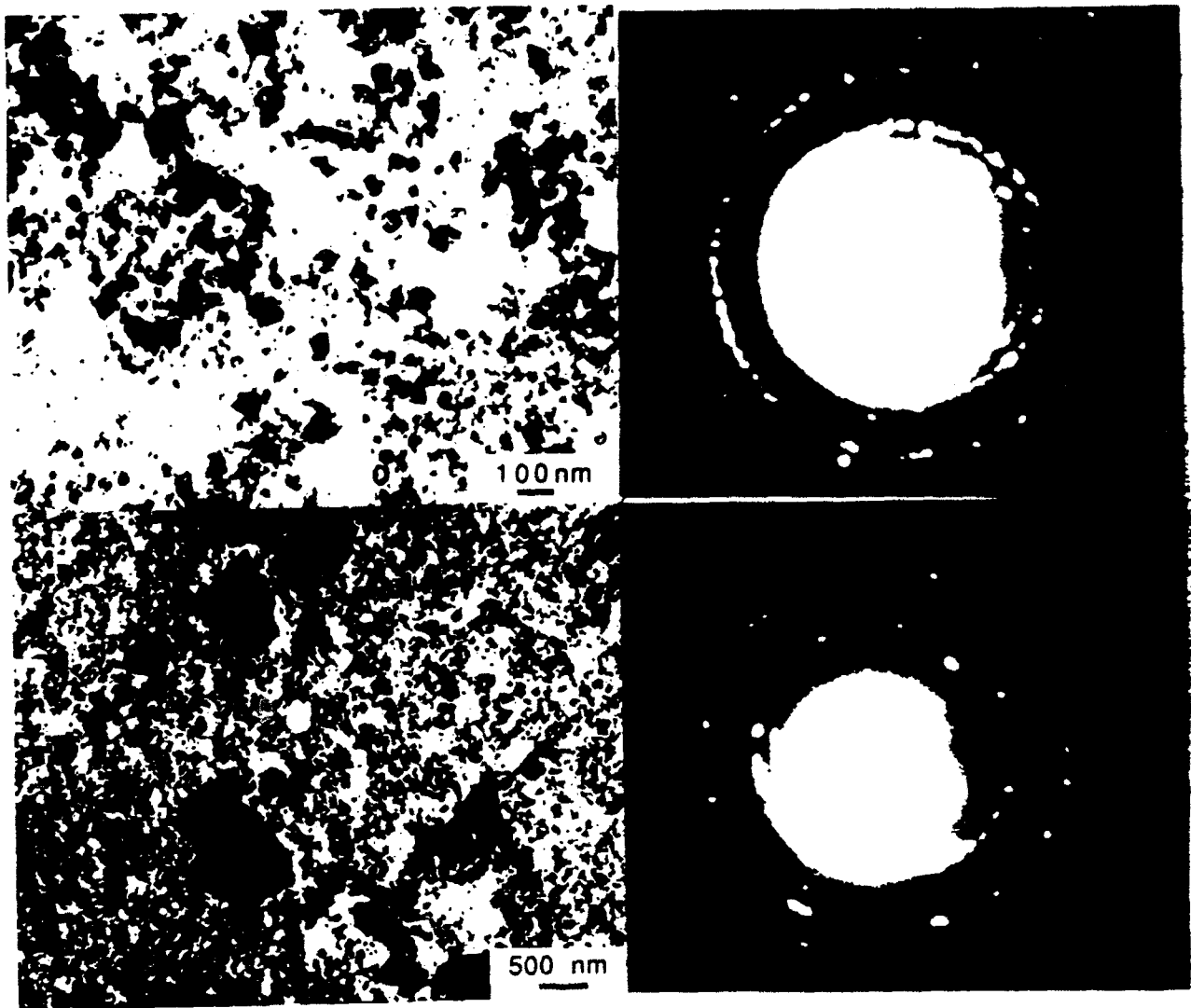(b) heated at 1173 K for 7.2 ks

(c) heated at 1273 K for 5.4 ks
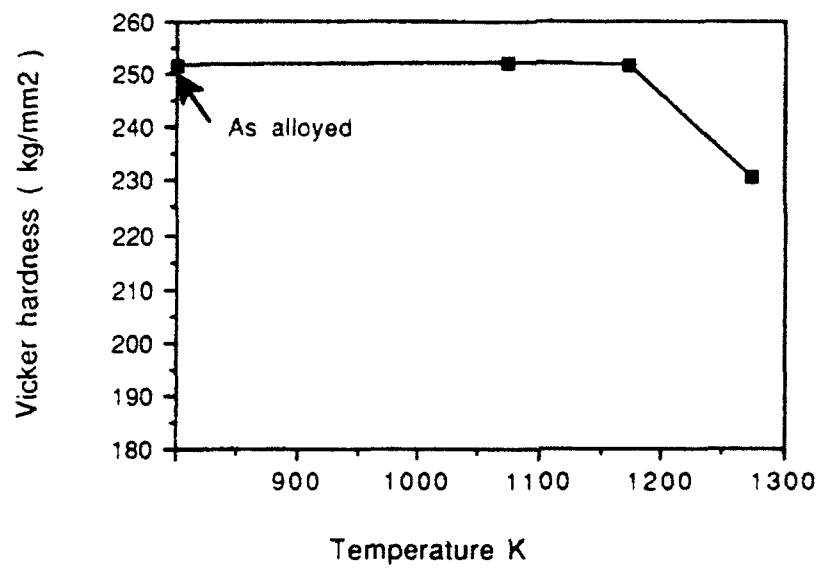
Fig. 4 TEM images of the dispersed TiN particles

Fig. 5 The room temperature hardness of Cu-TiN as a function
of annealing temperature

PROCESSING OF METAL MATRIX COMPOSITES

C. Persad, Z. Eliezer, D. L. Bourell, and H. L. Marcus,

Center for Materials Science and Engineering.

University of Texas, Austin, TX 78712

ABSTRACT

The use of powder constituents in the processing and fabrication of metal matrix composites provides diverse and flexible routes for the assembly of materials at the microscopic level. In the research that we describe here, the metal matrices were copper and tungsten. The dispersed phases were graphitic carbon, and boron carbide. Most of the processing was performed with the constituents in the solid state. In the high energy high-rate processing, energetic high-current pulses are directly applied to a powder mass to provide pulsed Joule heating. Heating rates of 1000 K/s to 10,000 K/s are achieved. When heat and pressure are simultaneously applied, rapid densification can occur. A homopolar pulse generator with 1 MA current capability has been used as a high current source. The investigation of binderless copper-graphite powder composites yielded materials with high densities, hardnesses and electrical conductivities. These materials have shown superior performance in terms of their high temperature capability and wear resistance in high current, high speed, electrotribological evaluation. The tungsten-based composite system offers a metallurgical cornucopia of phases including W, W_2C, FeWB, W_2B, Fe_3C, Fe_6W_6C, Ni_4B_3, and Fe_7W_6. These are obtained by reactions in the multicomponent system: W, Ni, Fe, B, C. Some of these phases have large heats of formation and the consolidation proceeds by exothermic heating under pressure. The processing science based on these approaches has as a common focus the understanding of the influence of basic processing parameters - time, temperature, and pressure - on the microstructure and properties of these composites.

KEYWORDS: Powder composite processing, high energy high-rate processing, Copper-graphite, Tungsten-Boron carbide, Evaluation/Testing

COMPOSITES

Design, Manufacture, and Application

Proceedings of the Eighth International Conference on Composite Materials (ICCM/8)
Honolulu, July 15-19, 1991

Edited by
Stephen W. Tsai and George S. Springer
Department of Aeronautics and Astronautics
Stanford University

1. INTRODUCTION

Of the many approaches developed for the processing of metal matrix composites (1), those based upon powder processing offer great flexibility in the selection and assembly of constituents. Conventional powder processing can be conveniently divided into primary operations such as mixing and blending, compacting and sintering; and secondary operations such as mechanical working and heat treatment aimed at developing near full density. Some of these primary and secondary operations are combined in new single-residence processes such as vacuum hot pressing, hot isostatic pressing, and quasi-isostatic processes such as rapid omnidirectional compaction and the Ceracon process (2). These offer a range of pressure-temperature-time combinations, which, when matched to particular materials systems, allow the investigation of a variety of materials responses.

Over the last few years a powder processing approach based upon the use of high energy electrical current pulses has been studied (3). This high-energy high-rate (HEHR) process has been applied to several composite materials including copper-graphite (4-7), aluminum-silicon carbide (8), nickel-molybdenum boride (9-10), and tungsten-based systems (11-14).

In this paper we review the results on the copper-graphite and W-Ni-Fe + B4C systems. These systems provide an interesting contrast in their processing responses. In the copper graphite system, the constituents have virtually zero mutual solubility and a stable copper carbide does not exist. The graphite is thus metallurgically inert with respect to the copper matrix yet contributes to solid state densification of the relatively soft copper matrix by accommodating strain and facilitating plastic flow. Easy shearing along the basal plane of the graphite particles enables this. In contrast, the W-Ni-Fe + B4C is a highly reactive system with a reaction temperature threshold reported to be 1173K (15). This threshold may be even lower ~ 1000K based upon the W+C reaction (16). Beyond these temperatures, the metallic constituents in this system consume all the available carbon and boron producing a rich array of carbides and borides, and in the process releasing significant heats of reaction.

2. PROCESS AND MATERIALS DESCRIPTION

2.1 HEHR Processing The high current source is a 10 MJ disk-type pulse homopolar generator. The homopolar generator (HPG) is an electric machine that converts rotational kinetic energy into electric energy using the Faraday effect. It is a low voltage, high current (1 MA) device that applies high energy pulses for a very short time. High energy/high rate (HEHR) consolidation of powders employing the homopolar generator as a power source has definite advantages over conventional powder metallurgy techniques. Since the energy is

delivered in a short time (about 1-3 seconds), this processing technique offers the opportunity to preserve the microstructure associated with the original powders in the consolidated material. Secondly, the energy deposition can be localized and concentrated at the interparticle contacts by manipulating film and contact resistances and the associated pulse Joule heating effect.
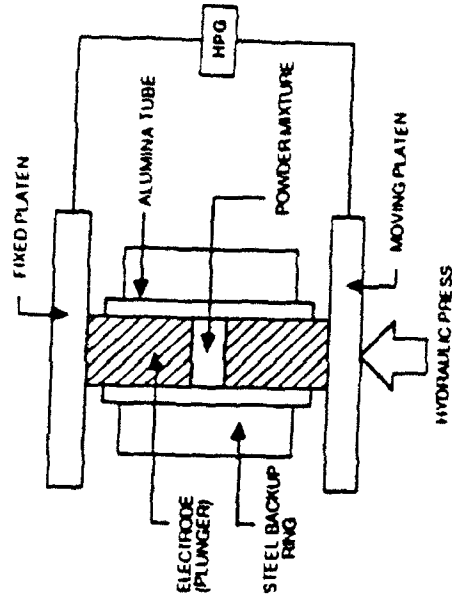

Figure 1. Schematic of the die arrangement employed in HEHR powder composite processing

A schematic sketch of the experimental setup is given in Figure 1. The steel backing ring was used to prevent the spreading of the die liner, which often cracks during the application of pressure and subsequent discharge of the pulse. The material used for die liner was alumina. The electrodes were made from ETP copper or 304 stainless steel. Die inserts, in the form of foils or disks, were placed between the electrodes and the compact to facilitate compact ejection. Insert diameter was equal to that of the electrodes. The inserts were molybdenum, niobium, or stainless steel foils, or molybdenum disks.

Powder temperature and pressure are controlled by adjusting the specific energy input and the hydraulic pressure respectively. The specific energy input (SEI) is the amount of energy in kilojoules per kilogram of the powder mass placed between the electrodes. The SEI was calculated using oscillographically recorded current and voltage vs time traces. The power at any instant, was calculated as the product of the current and the voltage. The total energy input was obtained as the integral over the total duration of the pulse.

2.2 Materials The copper powders were dendritic (< 325 mesh) and were combined with flake graphite powders in mass ratio of 89:11. Detailed characterization of these materials has been reported previously by Wang, et al. (5). The tungsten nickel iron + boron carbide were provided as a prealloyed and premixed blend. The metal matrix material had a W:Ni:Fe mass ratio of 93:5:2. The metal carbide mass ratio was 98.7:1.3

3. COPPER-GRAPHITE COMPOSITES

In the past, unidirectional graphite fibers/copper matrix composites have been extensively studied for use as electrical brushes. Although their behavior in the absence of current proved to be satisfactory, the passage of high currents increased the friction coefficient and the wear rate to unacceptable values; apparently, the lubricating properties of the graphite fibers are inferior to those of bulk graphite. One possible reason for that may be the desorption of water vapor from the graphite fibers at high interface temperatures (17). The substitution of the small-dimensioned fibers with powdered graphite to produce a copper + graphite powder composite was therefore pursued. Based upon promising microstructure/property combinations compared to commercial Cu-Cr-Sn-Pb composites, additional high-performance electrotribological systems are currently under development as indicated in Table 1.

Table 1. Materials systems being investigated for high-performance electrotribological applications.

Contact Type/ Constituents	Development Status	Performance/Characteristics
Composite Brushes		
Cu-Gr-Sn-Pb	Commercial Material	Used in present generation of pulse homopolar machines. Fails at 220 m/s due to catastrophic wear.
Binderless Cu-Gr	Experimental Material	Proposed for use in future pulse homopolar machines. Hardness and conductivity exceed that of commercial material.
Composite Armatures		
W-Cu(90/10)	Experimental Material	Hardness and conductivity exceed that of the 90W-10Cu commercially available material.
W-WC-C-Cu	Experimental Material	Nanosized constituents increase population of potential contact spots.

Preliminary results of the tribological characterization of the binderless copper and graphite powder based composites have been reported (4,7). The low speed pin on disk tests (0.6 m/s) of the copper and graphite on 4140 steel showed friction coefficients in the range 0.133 to 0.207 versus an average value of 0.120 for the commercial Cu-Gr-Sn-Pb composite. At high speeds the wear of the binderless composite is significantly lower than the commercial material. At 200 m/s values of 0.2-0.3 x 10^3 mm^3/Mm versus 2 x 10^3 mm^3/Mm, are obtained over 6 km sliding distance.

Table 2. Properties of composite materials for brushes

	Cu-Gr-Sn-Pb	Binderless Cu-Gr
Density (g/cm^3) (percent theoretical)	5.5	6.10-6.68
Average Hardness* (Rockwell 15T)	82.2	94.1-99.8
Electrical Resistivity (μ ohm-cm at 300K)	4.5	62 (Axial), 50 (Radial)
	37	3.82 (Axial), 8.95 (Radial)

* On this scale a fully dense copper powder compact has an average hardness of 70.7

Everett (18) reported on the pulse duty (<3 seconds) performance of these binderless copper graphite contact materials. An improvement in contact resistance was observed compared to commercial Cu-Cr-Sn-Pb composite material at velocities of 20m/s to 90m/s. Property comparisons of the commercial composite and the Binderless Cu-Gr given in Table 2, shows that latter material also has a lower bulk electrical resistivity. Current density comparisons at 100m/s and 160m/s showed the binderless material to have twice the current carrying ability of the commercial composite. When pulse loaded at 3kA/cm^2 at 160m/s, a nearly linear temperature rise of 100K/s was observed to a peak temperature of 420K.

The observed behavior depends strongly upon the intrinsic electrical conductivity of the composite material, and in particular of the copper matrix. One of the reasons for this is the limited exposure to elevated temperatures during processing. Figure 2, a plot of temperature vs time during consolidation of copper graphite, shows that the time above 0.4 Tm (270°C) for the copper matrix is about 5 seconds. This short time is significant for plastic deformation under the 420MPa applied pressure, without deleterious oxidation.
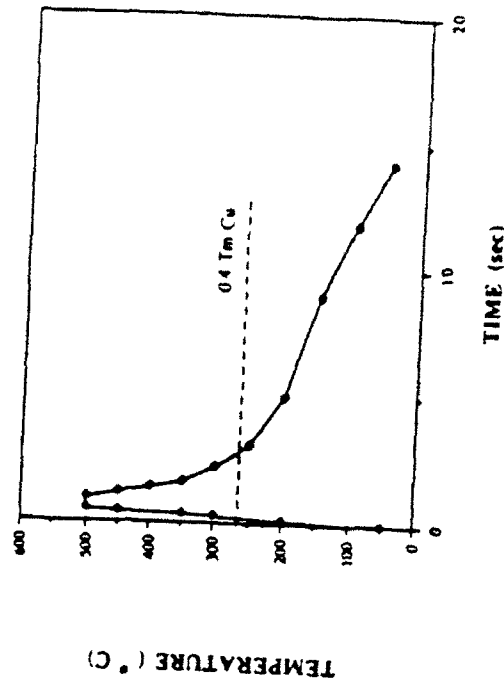

Figure 2. Observed temperature vs time plot for consolidation of a copper graphite powder composite to 95% density (P$_{max}$ = 420MPa)

One of the interesting features of these copper-graphite powder composites is their tailorable directional properties. Two orientations of the graphite particles depicted schematically in Figure 3 indicate the "edge-on" and "basal plane" orientations of the graphite in a copper matrix.

Performance testing of these composites indicated that lower operating temperatures and reduced wear rates are obtained when "edge-on" orientation is employed. Figure 4 provides a graph(on of the high temperature capability and the cooler operating temperatures observed in the "edge-on" orientation. (These temperatures were obtained by a contactless thermal imaging method with ±40°C error band.) We attribute this result qualitatively to the larger area available for metallic conduction through the copper in the "edge-on" orientation.

Edge-on Graphite Orientation   Basal-plane Graphite Orientation
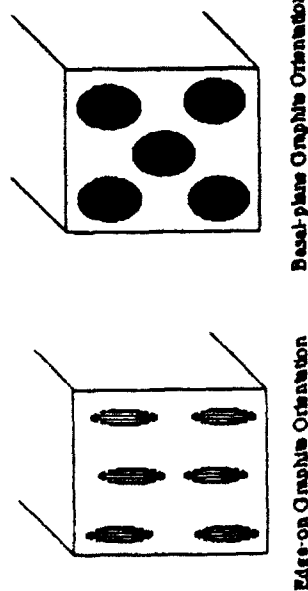
Figure 3.   Schematic depictions of copper-graphite contact surfaces showing roughly disk-shaped graphite crystals oriented in "edge-on" and "basal-plane" configurations.

Figure 4   Plot of maximum observed temperature vs downforce for copper-graphite composite sliding electrical contacts tested in the two orientations indicated in Figure 3. Test conditions: v = 200 m/s; j = 2 kA/cm², t = 30s.

Table 3   List of carbide formers (X) being examined and the methods by which they are introduced into copper-graphite composites

X	METHOD
Ti	Mechanical Alloying of Cu-Ti compositions from elemental powders. Ti-coating of graphite powders using Ti-ethoxide precursors
Cr	Mechanical Alloying of Cu-Cr compositions from elemental powders. Use of pre-alloyed Cu-Cr powders
Mo	Mechanical Alloying of Cu-Mo compositions from elemental powders. Mo-coating of graphite using molybdic acid precursors
W	Deriving Cu-W compositions from copper tungstates

For many sliding electrical contact applications, wear in the binderless copper-graphite may be reduced further by chemically bonding the graphite to the copper matrix. However, because of the dominance of the electrical heating component on the temperature rise of the contact during operation (see Figure 5), both the thermal and electrical conductivity need to be maximized. The baseline Cu-C powder composite system provides a vehicle for the comparative study of a Cu-X-C interactions, where X is a carbide former. In the table above we list some of the approaches being employed to the introduction of X into the baseline binderless copper-graphite composite. Some of these such as Cu-TiC are also model systems for basic interface design studies (19).

The potential effectiveness of these additions on improving the performance characteristics of copper based composite sliding electrical contacts depends upon a number of factors. Among these are their residual effect on bulk thermal and electrical conductivity, their influence on tribological behavior, and the bonding integrity of the carbide interfaces under thermal cycling.
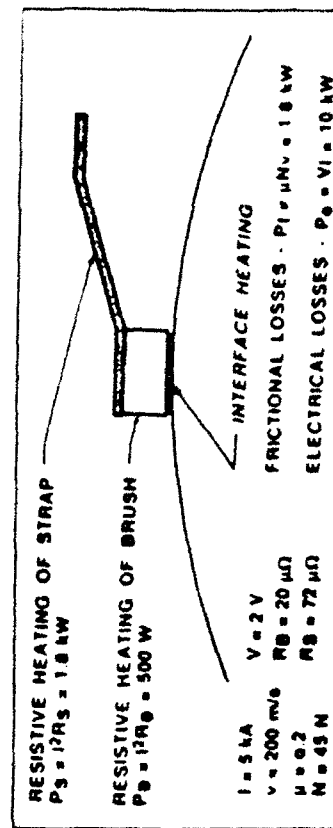

RESISTIVE HEATING OF STRAP
P$_S$ = I²R$_S$ = 1.8 kW

RESISTIVE HEATING OF BRUSH
P$_B$ = I²R$_B$ = 500 W

INTERFACE HEATING

FRICTIONAL LOSSES - P$_f$ = μNv = 1.8 kW

ELECTRICAL LOSSES - P$_e$ = VI = 10 kW

I = 5 kA   V = 2 V
v = 200 m/s   R$_S$ = 20 μΩ
μ = 0.2   R$_B$ = 72 μΩ
N = 45 N

Figure 5. Estimated contributions to the heating of an electrical contact carrying a 5kA current

INTENSITY

2 θ (DEGREES)

Figure 6. X-Ray diffractographs comparing spectra obtained for (a) W-Ni-Fe + B₄C powders prior to processing. (b) Processed in the solid state under 210MPa pressure. (c) Processed with liquid phase assisted flow at 420MPa pressure

4. TUNGSTEN-BASED COMPOSITES

Pressures of 210MPa and 420MPa were applied to the powders and energy inputs were 3700kJ/kg to 4000kJ/kg. At the lower pressure, densities of 92% to 93% were obtained. The constituents remained in the solid state and the B₄C phase was retained. At the higher pressure, a density of 97% was obtained apparently through liquid-phase-assisted consolidation and the B₄C was fully reacted. Figure 6 compares the XRD patterns of the starting powders (a) and of the solid-state processed material (b) and that in which a liquid phase was formed (c).

The liquid-phase-assisted consolidation products are especially noteworthy. The EDS analysis of the metallic constituents in the matrix revealed a mixture of tungsten, nickel, and iron. The average composition of the matrix obtained from different locations in the matrix was 85.1 wt. % W, 10.3 wt. % Ni, and 4.6 wt. % Fe. Based on x-ray diffraction analysis, the phases identified were W, W₂C, FeWB, W₂B, Fe₃C, Fe₆W₆C, and Ni₄B₃. The intermetallic Fe₇W₆ was also observed. These reaction products were not observed in compacts consolidated at lower pressure, where the constituents seemed to have undergone solid-state consolidation.

At 420 MPa applied pressure, the boron carbide seemed to have reacted completely and the resulting complex borides and carbides were homogeneously dispersed. The matrix was homogeneous with the W : Ni : Fe ratio being approximately the same at different locations in the matrix. This process has the characteristics of "self-propagating high-temperature synthesis" or "SHS" (16). SHS is a reaction where an exotherm is involved thereby liberating thermal energy. This liberated heat helps sustain the reaction for a longer time without any external heat input. Material systems with SHS potential offer the possibility of using appropriately tailored electrical current pulses to bring a multitude of microscopic reaction zones to the threshold of self-propagation and then allowing the exothermic heating to activate full densification. This approach is currently being pursued in the Cu-W-C system.

Recently, studies of nanocomposites based upon W-W₂C have been undertaken. In the W-W₂C system, the synthesis/processing approach is centered around developing means for producing stable ultrafine-grained compositions. One of the composite powder synthesis routes being employed is the reduction and carburization of tungstic acid gels in flowing hydrogen and methane atmospheres. This effort extends the results previously obtained in microstructure control of ultrafine-grained tungsten powders form gel precursors (13).
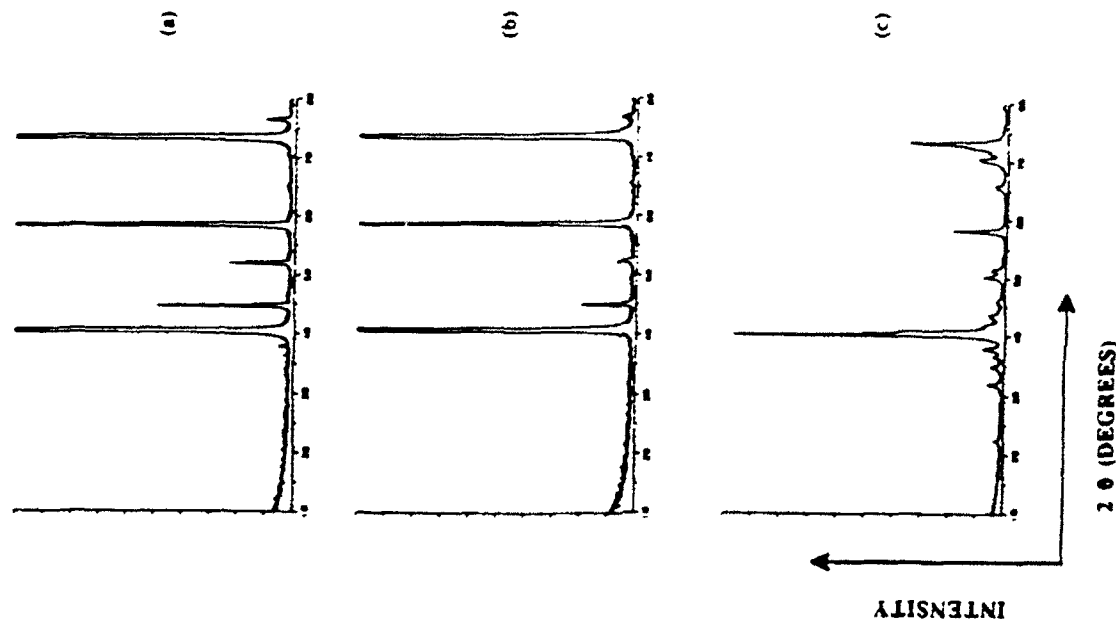
VIBRATION EXCITATED LOW PRESSURE CASTING; A NEW ROUTE TO PRODUCE METAL MATRIX COMPOSITES.

I. O Prunander *, J. F. Ståhl * and C. H. Andersson **.
Department of Production and Materials Engineering,
Lund Institute of Technology *
Box 118, S-221 00 Lund, Sweden

Swedish Institute for Textile Research, TEFO **
Box 5402, S 402 29 Göteborg, Sweden

1 March 1991

ABSTRACT

This paper presents the principles and some properties of composites made by a new low pressure route to produce preform based metal matrix composites.

The problems of getting a preform infiltrated by molten metal are well known. The use of high pressure in combination with high temperature enables infiltration of fibre preforms. However, that kind of approach also often activate chemical attacks, gives some remaining porosity with gases entrapped at high pressure and uncontrolled deformation of the fibre preform.

By the use of low applied pressure, it is possible to avoid the uncontrolled fibre distribution and preform breaks of composites made by conventional high pressure squeeze casting.

For the use of low applied pressures for wetting of the preform is needed. This is done by high energy vibrational geometrical barriers for infiltration, however, some kind of energy to overcome the assistance of the casting. Thus, temperature less than 100°C above liquidus can be used for Al alloys too.

Deformation of preforms less than 1% and very low fractions of porosity are obtained in the composites.

Infiltration front velocity of the molten metal matrix has been detected and registered contin uously during casting. Data can best be interpreted in terms of metastable equilibrium models in which an advancing liquid front has to overcome energy barriers associated with geometrical features.

KEYWORDS: Composites : matrix/aluminium/preform ; manufacturing/vibration/low pres sure.

5. REFERENCES

T. W. Clyne, in F. L. Matthews, et. al., eds., Proceedings of the Sixth International Conference on Composite Materials, Elsevier, London, 1987, pp 2275-2286.

Metals Handbook, Vol. 7, Powder Metallurgy, ASM, Metals Park, 1984, pp. 537-550.

H. L. Marcus, D. L. Bourell, Z. Eliezer, C. Persad, and W. Weldon, Journal of Metals, 39, (12), 6 (1987).

K. C. Owen, M. J. Wang, C. Persad and Z. Eliezer, Wear, 120, 117 (1987).

M. J. Wang, C. Persad, Z. Eliezer, and W.F. Weldon, in J. Gully, ed., Proceedings of the 3rd Int. Current Collector Conference. Austin, TX, Nov.1987, paper #20.

Z. Eliezer, M. J. Wang, C. Persad, and J. H. Gully, in , C. C. Sorrell and B. Ben-Nissan, eds., Ceramic Developments Materials Science Forum, Vol. 34-36, Trans Tech Publ. Switzerland, (1988) pp. 505-509.

C. Persad, et. al., in P. K. Rohatgi, P. J. Blau, C. S. Yust, eds., Tribology of Composite Materials, ASM International, Materials Park (1990), pp. 203-216.

H. L. Marcus, et.al., in F. L. Matthews, et. al., eds., Proceedings of the Sixth International Conference on Composite Materials, Elsevier, London, 1987, pp 2459-2467.

Y. W. Kim, D. L. Bourell, and C. Persad, Journal of Materials Science and Engineering, A123, 99 (1990).

Y. W. Kim, L. Rabenburg, D. L. Bourell, Journal of Materials Research, 3 (6), 1336 (1988).

C. Persad, et. al., "High-Energy High-Rate Processing of High-Temperature Metal-Matrix Composites," MRS Symposium Proceedings, 120, 23 (1988).

C. Persad, et. al., Proceedings of the Tenth Inter-American Conference on Materials Technology, IIE/OAS/SwRI, San Antonio, (1989), Vol. II, Section 30, pp. 33-39.

C. Persad, et. al. in A. H. Clauer and J. J. Barbadillo, eds., Solid State Powder Processing, TMS, Warrendale (1990), pp. 357-364.

S. Raghunathan, et. al., J. Materials Science and Engineering, A131, 243 (1991).

H. Sheinberg, in G. S. Upadhaya ed., Sintered Metal-Ceramic Composites, Elsevier, Amsterdam, 1984, pp. 377-398.

A. Muniz, Ceramic Bulletin, 67 (2), 142 (1988).

Z. Eliezer, in K. Friedrich, ed., Fraction and Wear of Polymer Composites, Elsevier, 1986.

J. Everett, MS Thesis, The University of Texas at Austin, Dec. 1988.

M. E. Fine et al., Scripta Metallurgica, 22 (6), 907 (1988).

Development of a Selective Laser Reaction Sintering Workstation

B.R. Birmingham, J.V. Tompkins, G. Zong, and H.L. Marcus

Center for Materials Science and Engineering
The University of Texas at Austin
Austin, Texas 78712

Abstract

The purpose of this paper is to describe the design and operation of a Selective Laser Reaction Sintering workstation developed at The University of Texas. The workstation allows the study of solid freeform fabrication of reaction sintered materials on a research scale. The mechanical and control systems of the workstation are detailed, and Selective Laser Reaction Sintering as a technique is discussed including example material systems that are currently under study.

Introduction

Solid freeform fabrication (SFF) is any manufacturing process that produces a three dimensional part without the use of standard or part specific tooling. One form of SFF, Selective Laser Sintering (SLS), uses a laser to sinter selected areas of a powder bed. Additional layers of powder are spread on top of the first, and specific areas of each layer are scanned and sintered by the laser before the next layer is spread. In this way, a three dimensional sintered part is built up layer by layer. At the end of the process, the manufactured shape may be removed from the surrounding loose powder. Parts have been made from various polymers, metals and ceramics using this technique [1,2]. Selective Laser Reaction Sintering (SLRS) combines SLS with a simultaneous gas/powder reaction process known as reaction sintering or reaction bonding[3]. This simultaneous reaction typically involves the decomposition of a gas to solid or a gas interacting with a liquid or solid to produce another solid. The SLRS process has the potential of producing parts made of monolithic materials and composites that are difficult or impossible to sinter using SLS as well as producing microstructures that are unobtainable using standard sintering techniques.

Equipment

To be successful a SLRS system must accomplish three basic functions. These functions are 1) supply controlled laser power to a selected area, 2) provide multiple layers of a powder bed having proper thickness and density and 3) provide the

appropriate gas environments including vacuum. An overall schematic of the SLRS system is seen in figure 1.
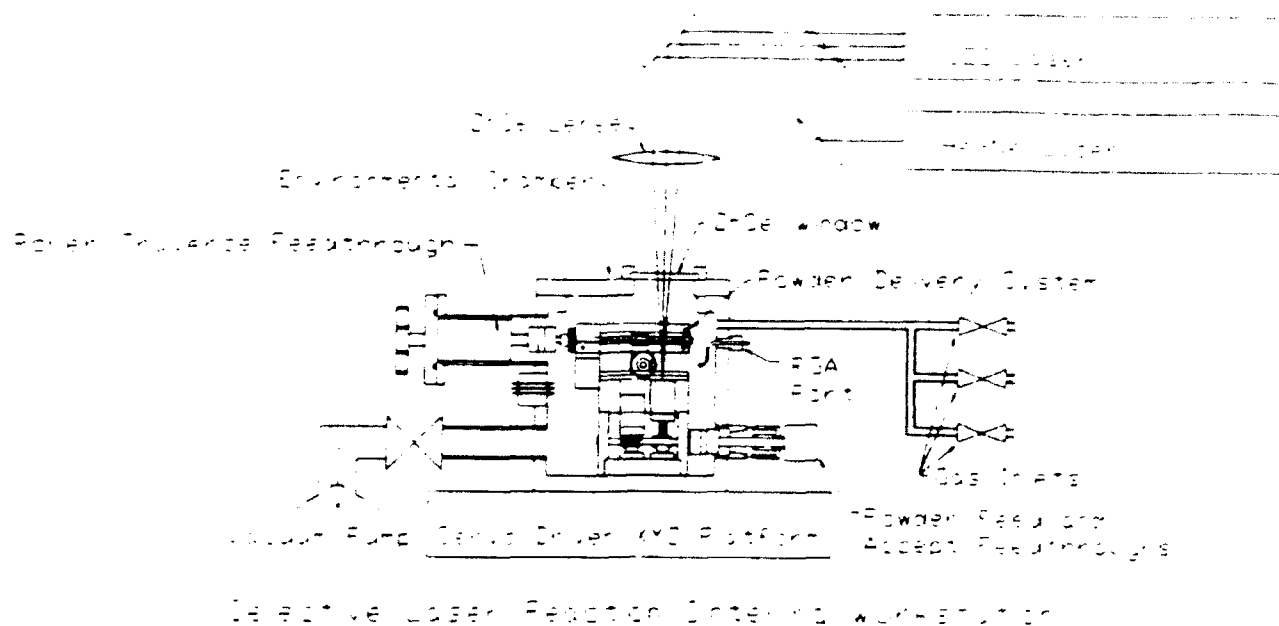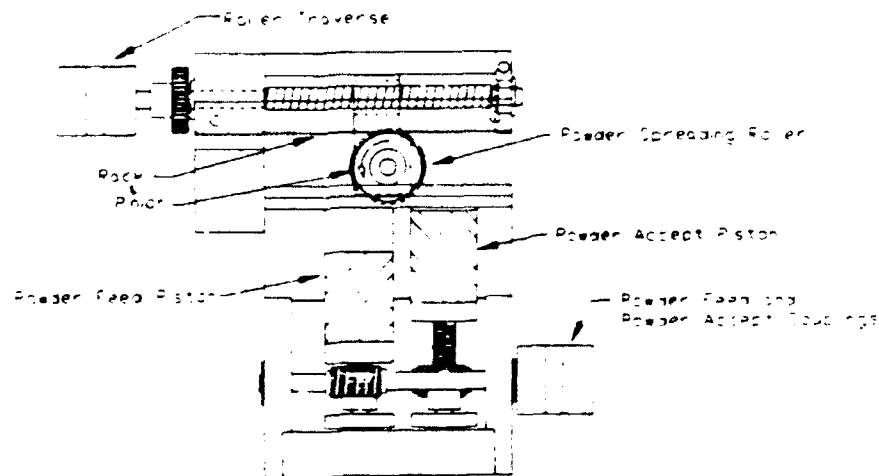

Figure 1.

With the exception of the powder delivery mechanism, the basic arrangement of this system has been previously described in the literature [3]. The laser beam from a 25 watt CO_2 laser is directed onto a substrate that is located in an environmentally controlled chamber. A motor driven X-Y table moves the chamber/substrate under the stationary beam effectively "scanning" the beam. Both laser power and X-Y table controls have been upgraded for this workstation. Laser power fluctuations have been reduced to less than 5% of setting by using a pulse width modulation controller developed at the University [4]. Power level can be adjusted manually or by computer. Positional accuracy of the table/beam is now better than $20\mu m$ and repeatability better than $5\mu m$ at scan speeds to 3mm/sec using a computer controlled dc servo system.

Environmental control is achieved by locating the powder delivery mechanism/substrate inside a vacuum chamber. The chamber has three independent gas inputs with the emphasis on flexibility due to the research nature of the system. The gas inputs have allowed for the introduction of a variety of gases including N_2, N_2/H_2, NH_3, Ar, H_2, O_2, CH_4, and C_2H_2. The chamber is currently set up for static gas environments, but minor modifications could easily make it a flowing gas system if desirable. Mechanical pumping initially provides 10^{-3} Torr vacuum to minimize gas impurity content. Mechanical and resistance vacuum gauges monitor system pressure. Power and thermocouple feedthroughs provide the ability to heat substrates and monitor and control temperature using a PC based data acquisition system. A gas sampling port has also been included to enable connection to a gas analyzer system(RGA). This will be used to gather information about reactants and by-products during the reaction sintering process. Mechanical feedthroughs currently enable manual operation of the powder delivery mechanism. The mechanism will be automated in the future.

2

The powder delivery system is similar in concept to one previously reported [5], but considerable miniaturization was required to fit the entire mechanism inside the available five inch diameter by 5 inch in height vacuum chamber . A schematic and photograph can be seen in figures 2 and 3. Two rotation feedthroughs marked Powder Feed and Powder Accept are coupled to worm/gear/leadscrew arrangements that ultimately drive the powder feed and powder accept pistons up and down in their respective cylinders. The rotation feedthrough marked Roller Traverse drives a spur gear/leadscrew arrangement that causes the roller to traverse across the top of the stage.

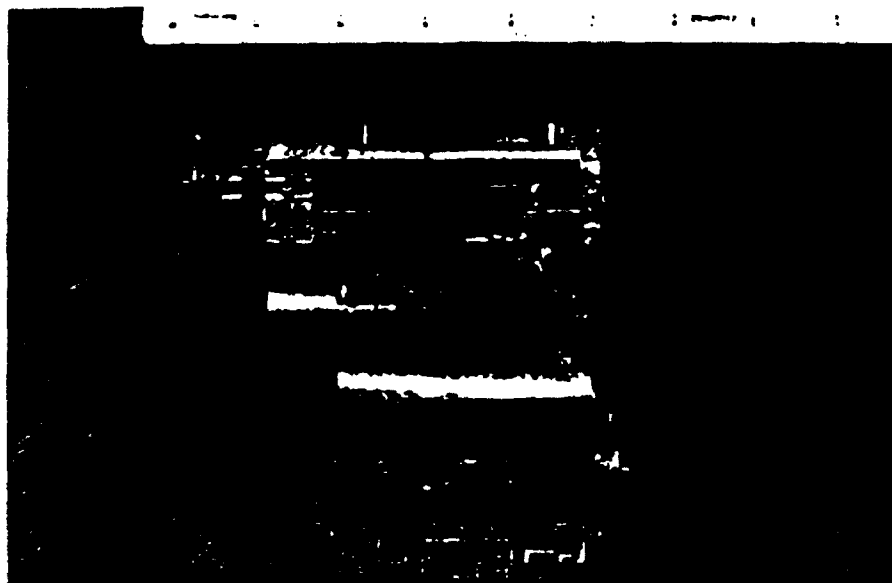
Powder Delivery System

Figure 2.

Figure 3.

During a standard production cycle the system starts with the traversing roller to the far left, the powder feed piston would be down and its cylinder full of powder, and the powder accept piston would be up. Powder is made available to the roller by raising the powder feed piston an incremental amount. The roller is then traversed across the

stage and then back, spreading the powder into a thin layer. As the roller traverses, a rack and pinion causes the roller to spin so that the roller surface in contact with the powder is actually moving in a direction opposite to traverse direction. This is done for improved powder spreading. After the new powder layer is spread, a laser scan is performed, sintering specific areas of the powder layer above the powder accept piston. When the scan is complete, the powder accept piston is lowered some specified layer thickness. The powder feed piston is again raised, providing another incremental amount of powder. The roller is brought across the stage, spreading a fresh layer of powder over the powder accept piston and the previously sintered layer. The laser is scanned again resulting in a second sintered layer. The powder accept piston is lowered and the process is repeated until the part has been built up layer by layer. Maximum part size from this mechanism is roughly a 1.5cm by 1.5cm by 1.5cm cube. The gearing of the mechanism enables layer thickness control to within a few microns. Working on this scale is advantageous when using difficult to make, hazardous or expensive materials because of the small amounts of precursor required to load the system. When the materials systems have been proven on this scale they can easily be adapted to a larger system.

Applications

Laser reaction sintering can be used in a variety of ways to produce a variety of results. The following discussion is by no means all inclusive, but is meant to give examples demonstrating some of the interesting aspects of this technique.

Standard pressureless sintering of oxides, nitrides, and carbides is difficult. However, formation of an oxide, nitride or carbide may be achievable by reaction sintering in the corresponding oxygen, nitrogen, or carbon rich atmosphere. One example is the reported success of sintering an aluminum/alumina mixture in the presence of oxygen to form an alumina pre-form [6]. These pre-forms will be infiltrated to create a metal-ceramic or ceramic-ceramic composite part.

Composite structures can be produced directly by partial conversion of powder by reaction. A multi-layer Cu-TiN part was produced by this SLRS system using a Cu-10Ti alloy as base material. Reaction sintering in a nitrogen atmosphere caused the Ti to migrate to the surface of the alloy particles where it reacted with nitrogen to convert to TiN. The result was a copper matrix with a sub micron TiN layer on each of the original powder particles. TiN presence was confirmed by x-ray diffraction and the dispersion of Ti rich areas(TiN) was mapped using EDS. Figure 4 shows a side view of a 6mm by 6mm by 3mm thick Cu-TiN rectangular solid made using SLRS. Note that the part is composed of 15 layers. The delamination observed can be eliminated with proper substrate pre-heating. The microstructure of the part can be seen in Figure 5, which contains a backscattering electron micrograph and a Ti element map of the same region. The element map clearly shows the Ti migration to the surface of the alloy particle where it formed a nitride coating on the particle. It is believed that proper control of powder size and operating parameters can result in very fine microstructures unobtainable by standard sintering techniques.
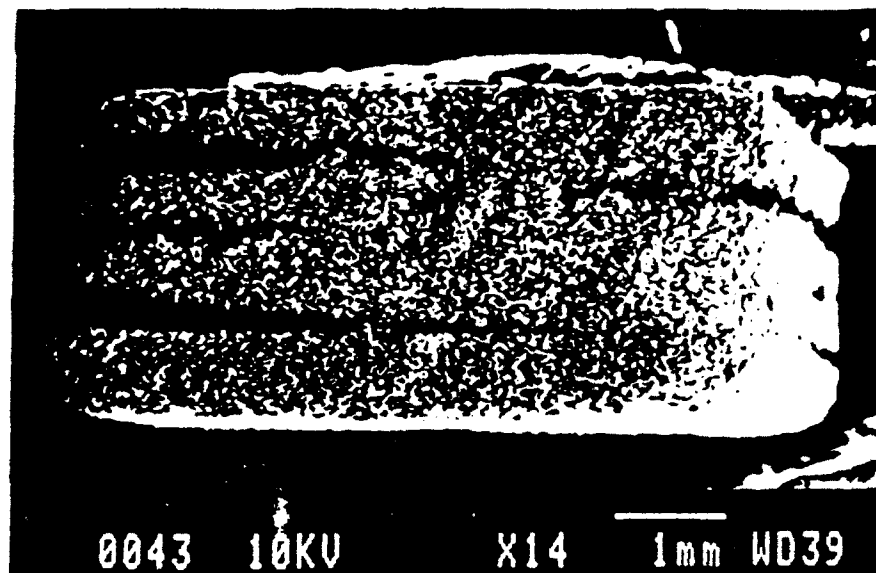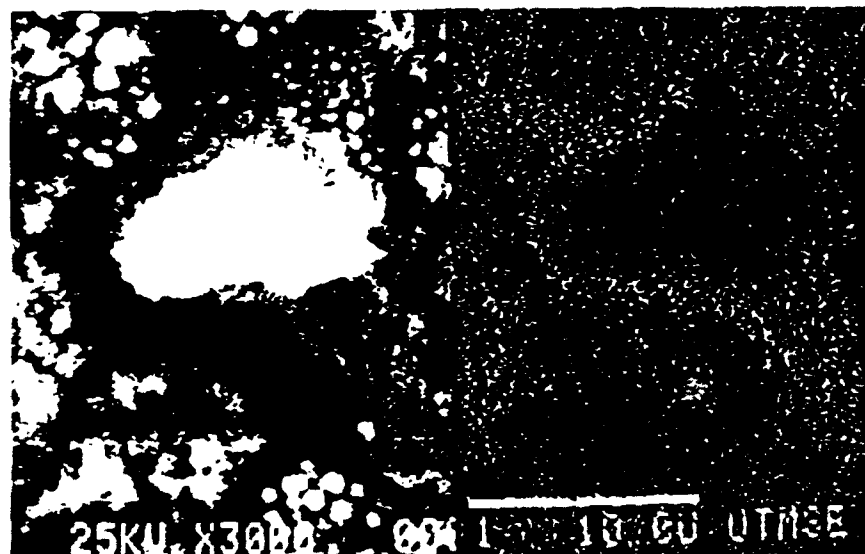
Figure 4.

Figure 5.

A third technique involves laser sintering and simultaneous vapor deposition and infiltration. One system currently under study combines the pyrolitic formation of SiC from an organometallic gas precursor with the sintering of a SiC base powder. The pyrolitically produced SiC infiltrates the SiC base powder and binds it together. Single and multi-layer parts have been formed in this fashion. Figure 6 shows the side view of a single layer of SLRS SiC. Starting powder was 16μm SiC. Note the density variation through the layer. Figure 7 is the top view of a 6mm square by 1mm thick SiC rectangular solid. The six layer part was also made using 16μm SiC. Bonding between the layers is limited, but it is believed this can be improved by optimization of process parameters including laser power, gas pressure, powder size and layer thickness.
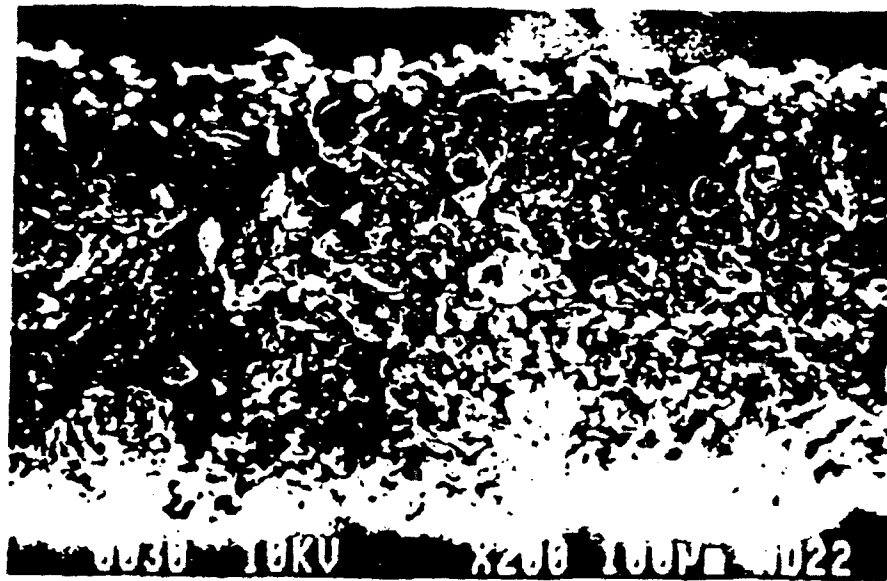
Figure 6.
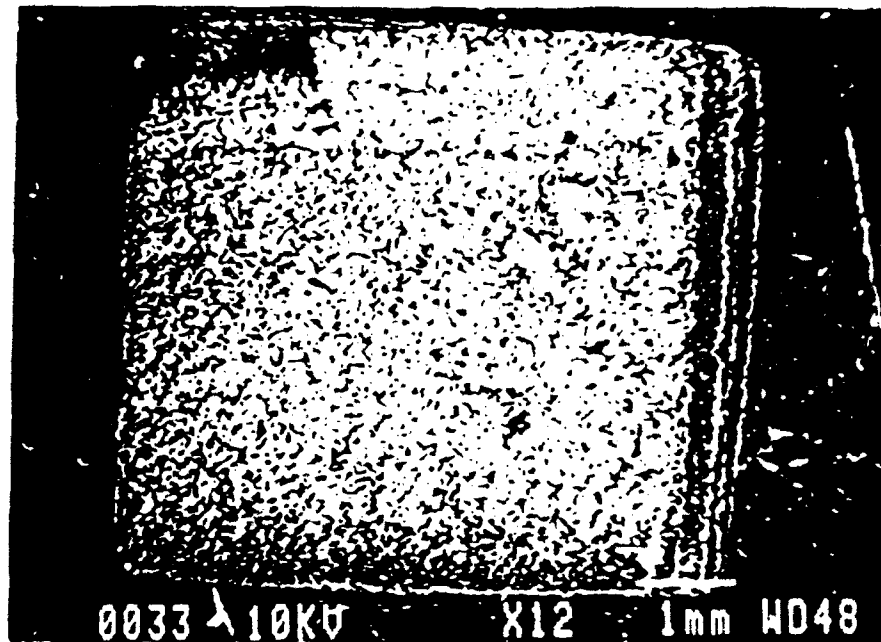
Figure 7.

Conclusions

A Selective Laser Reaction Sintering workstation is in place and operational. It is capable of producing multi-layer solid freeform parts in an environmentally controlled chamber. This will enable the study of laser sintering combined with gas phase/powder reactions. It is believed that this combination is capable of producing materials and structures unobtainable by standard sintering techniques. Preliminary studies are positive.

Acknowledgments

References

1   Harris L. Marcus, Joseph J. Beaman, Joel W. Barlow, and David L. Bourell, "From Computer to Component in 15 Minutes: The Integrated Manufacture of Three-Dimensional Objects," JOM,42[4], 1990,pp. 8-10.

2   "Rapid Prototyping Systems," Mechanical Engineering, edited by Steven Ashley, April 1991, pg 41.

3   M.E. Washburn, W.S. Coblenz,"Reaction-Formed Ceramics," Ceramic Bulletin, Vol 67, 2, 1988, pp. 356-363.

4   Guisheng Zong, R. Carnes, H.G. Wheat, and H.L. Marcus, "Solid Freeform Fabrication by Selective Area Laser Deposition," Proceedings of the Solid Freeform Fabrication Symposium, Austin, Texas, August 6-8, 1990, pp. 83-90.

5   J.V. Tompkins, "Computer Control of Laser Intensity for Selected Area Laser Deposition," Masters Thesis, University of Texas at Austin, Austin, Texas, 1992

6   C. Deckard and J.J. Beaman; pp. 623-629 in Advances in Manufacture, Integration and Processes, Proceedings of the 15th Conference on Production Research and Technology, Berkeley, California, January 9-13, 1989. NSF Design, Manufacturing and Computer Integrated Engineering Division, Washington D.C., 1989.

7   P.K. Subramanian, G. Zong, and H.L. Marcus, "Selective Laser Sintering and Reaction Sintering for the Fabrication of Ceramic Composites," Proceedings of The Solid Freeform Fabrication Symposium, Austin, Texas, August, 1992.

Residual stress effect on impact properties of Gr/Al metal matrix composite

JI-LIANG DOONG
Department of Mechanical Engineering, National Central University, Chung-li, Taiwan 32054

SHYH-NUNG S. LIN, H. L. MARCUS
Center for Materials Science and Engineering, The University of Texas at Austin, Austin, TX 78712, USA

The effects of residual stress on the impact properties of the unidirectionally reinforced P 100 Gr/6061 Al metal matrix composites with different thermal histories have been investigated using an instrumented impact test method and scanning electron microscopy. The cantilever impact generally causes tensile failure at the notch and compressive loading on the opposite side of the specimen. The specimens with yield tensile matrix residual stresses have planar fracture surfaces and low impact energy due to the contribution of tensile residual stress. The specimens with small residual stresses have moderate impact energy because debonding between fibre and matrix or fibre/matrix separation also serves as an additional mechanism for energy absorption. The specimens with higher compressive matrix residual stresses have the largest maximum load of all the specimens with the same matrix treatment. The specimen with matrix compressive yield residual stress has the maximum impact energy owing to a stepwise fracture surface. It can be concluded that good impact properties of composite materials can be obtained by choosing a suitable thermal history to modify the deleterious tensile matrix residual stress.

1. Introduction

Metal matrix composites (MMC) provide a relatively new way of strengthening metals and they are recognized to have the potential for high-temperature application while maintaining usable levels of fracture strength. However, a residual thermal stress can build up because of a difference in thermal expansion coefficients of the fibre and the matrix when cooling from high processing temperatures. Owing to the large thermal mismatch in the fibre longitudinal direction, the thermal stress can be large enough to cause yielding in the matrix. For example, the combination of graphite fibres with slightly negative coefficient of thermal expansion (CTE) and aluminium matrix with high positive CTE leads to a plastic flow in the matrix and large internal stresses in the constituents even for a relatively small temperature change [1]. The estimation of residual stress is required to evaluate the performance of MMC. There have been a few studies [2-5] to estimate the thermal residual stresses. Some research has focused on experimental measurements of residual stresses [6-8]. It is well recognized that the state of stress affects the performance of these composites. The effect of the thermally induced residual stresses on the yield behaviour has been discussed by Wakashima *et al.* [9]. However, there has been very little work reported on the effects of residual stresses on dynamic responses of MMC materials.

Understanding the impact response of composites has become an area of great academic and practical interest [10-14]. It is well known that the mechanical properties and the fracture mechanisms of composites with residual stresses are different from those of materials without residual stresses, because of the superimposition effect of the residual stresses with the applied stresses. In addition, fibre composites are highly susceptible to internal damage caused by impact loading. It is therefore necessary that this effect should be studied in more detail.

The impact response of composites reflects a failure process involving crack initiation and crack growth in the elastic plastic matrix, fibre breakage and pull-out, delamination, and debonding. The instrumented impact test is potentially a more useful tool for evaluating the dynamic response of materials mainly because the traditional Charpy and Izod impact tests could not provide such information. The force-displacement curves of the test specimen during impact can be recorded by a computer-controlled data acquisition system and then analysed. The shape of the curve provides information on the initiation, yielding, and propagation energy during impact.

The purpose of the present study is to investigate the effects of thermal residual stresses on the impact properties of MMC P 100Gr 6061Al using an instrumented impact tester. The test specimens with various

residual stresses can be obtained via heat treatments of the aluminium matrix composite. Scanning electron microscopy is applied to study the microstructural failure mechanisms.

2. Experimental procedure

A unidirectionally reinforced double-ply pitch P 100 Gr 6061 Al MMC plate for this study has a total thickness of 0.81 mm, with 6061 Al face sheets of thickness 0.1 mm on both sides. Fibre volume fraction of the composite, V_f, is about 40%. A detailed description of residual stress estimation by X-ray diffraction was presented elsewhere [15, 16]. The specimen number, thermal histories, and residual stresses are shown in Table I.

The drop-weight impact tests were conducted on a Dynatup Model 8200 with GRC 730-I automated data acquisition and analysis system. The striking tup and the anvil of the tester were designed according to the ASTM standard for Charpy test. The specimen dimensions were 80 mm long by 10 mm wide and a 2 mm depth notch was machined at the centre of the length. The hammer and tup weighed 9.55 kgf. The impact velocity was set at 1.83 m s^{-1}. The critical parameters which were used to compare the impact response of each material include: (a) maximum load, P_m; (b) energy absorbed to maximum load (end of damage initiation phase), E_m; (c) total absorbed energy for through-penetration, E_t; and (d) the energy absorbed in the propagation phase, $E_p = E_t - E_m$ and the ductility index, DI, equal to E_p/E_m. The measurement data are summarized in Table II and typical impact response of force-time diagrams are shown in Fig. 1.

A Jeol 35 SEM using a 25 keV primary beam was used for the microstructural studies. The specific features in the micrographs of each tested specimen will be discussed in the next section.

3. Results and discussion

3.1. Residual stress effect

The previous microstructural studies [15, 16] revealed that maximum residual stresses of the composite were determined by the yield strength of the aluminium matrix which was different from the monolithic alloy.

The maximum residual stresses measured at any quenching temperature are approximately 100 and 140 MPa for Al-T4 and Al-T6 treatments, respectively. The residual stresses measured in the aluminium alloy matrix were found to be in good agreement with the calculated results of Rice et al. [17] using finite element methods. The stress of the fibre is opposite to that of the matrix [18, 19]. For the case of uniaxial, uniform displacement, thermal stress changes in both phases. The approximate relationship between the matrix stress change, $\Delta\sigma_m$, and fibre stress change, $\Delta\sigma_f$, can be expressed as

$$\Delta\sigma_f V_f = -\Delta\sigma_m (1 - V_f) \qquad (1)$$

For these composites with $V_f = 0.4$, the residual stress of the fibres is opposite to that measured in the matrix with a magnitude of 1.5 times as large. It means that interfacial shear stress between fibre and matrix increases with the matrix residual stresses. For example, the residual stresses of specimen with T6-1 treatment are 140 and −210 MPa for matrix and fibre, respectively. The stress difference is 350 MPa. For a specimen with T6-3 treatment, the stress difference is only 15 MPa. In addition, interface debonding will occur if the interfacial bonding is not strong enough to withstand the shear stress resulting in the pull-out phenomenon. All these cause the failure of the composite materials. Therefore, the residual stress of composites should be reduced to as low as possible. Owing to the superimposed effect of residual stresses on the applied load, the compressive residual stress has a retarding effect on fatigue crack growth [20, 21].

The cantilever impact on the specimens causes tensile failure at the notch and compressive loading at the surface opposite to the notch. The crack initiation and propagation occurs at the notch. Thus when compressive residual stresses are present in the matrix, the applied stress must overcome them first so that the fracture can take place. In contrast, tensile residual stresses in the matrix accelerate the fracture.

3.2. Impact response

Golovoy et al. [22] investigated the impact response of laminate composites and indicated that tensile failure is the major mechanism in the initiation stage. Fracture propagation involves both tensile and shear

TABLE I Residual stresses of graphite fibres in P100/6061 Al matrix with various thermal histories

Specimen number	Solution treatment (C)(h)	Ageing treatment (C)(h)	Quenching* temperature (C)	Residual stress (MPa)
T4-1	530/2	None	200(RT)	93
T4-2	530/2	None	−78.5	3
T4-3	530/2	None	−117.0	46
T4-4	530/2	None	196.0	−78
T6-1	530/2	160/18	200(RT)	140
T6-2	530/2	160/18	−78.5	30
T6-3	530/2	160/18	−117.0	−6
T6-4	530/2	160/18	196.0	30

* Four different thermal histories were used with various quenching temperatures after ageing treatment and then back to room temperature (20 C).
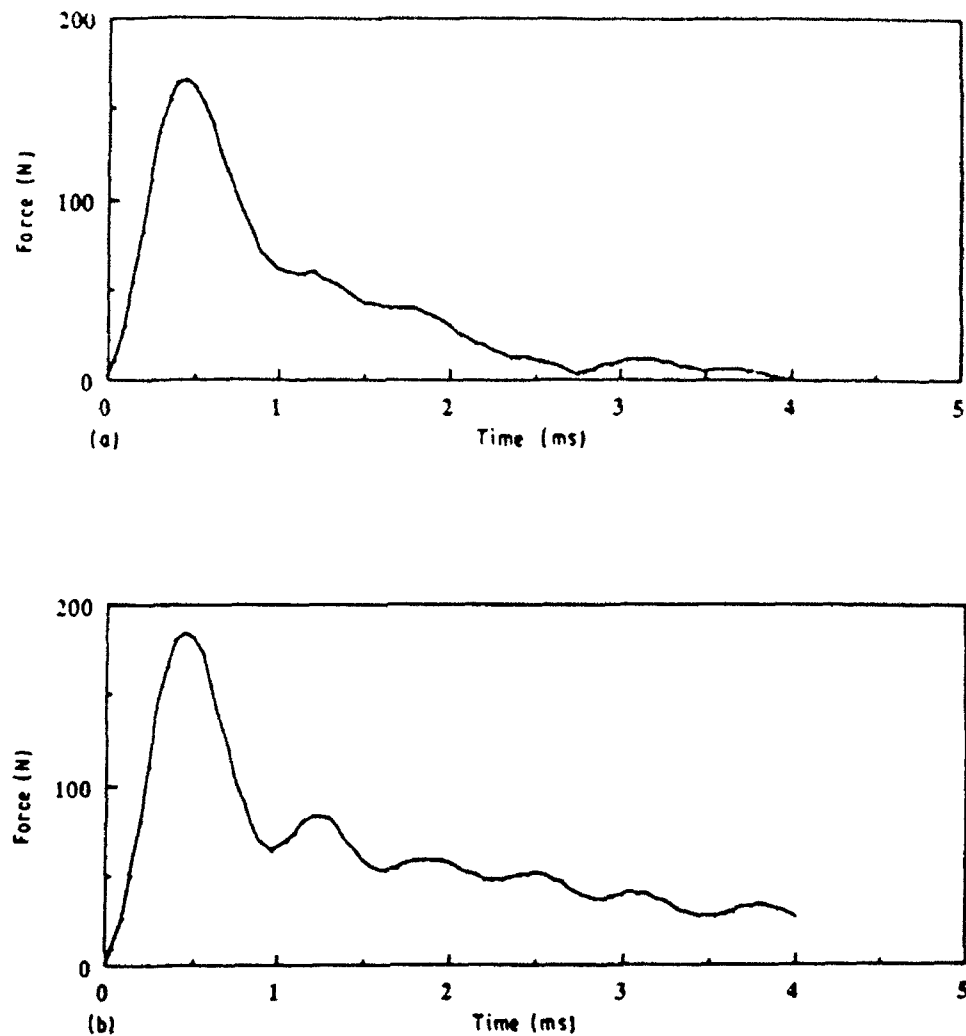
Figure 1 The force-time-impact response diagrams of specimens (a) T4-1, (b) T4-4.

TABLE II The effect of residual stress on the composite impact properties

Specimen number	Maximum load (N)	t_m (ms)	E_m (J)	E_p (J)	E_t (J)	DI
T4-1	180.58	0.350	0.0758	0.2144	0.2902	2.8298
T4-2	195.60	0.350	0.0691	0.5798	0.6489	8.3957
T4-3	199.34	0.350	0.0817	0.3697	0.4514	4.5238
T4-4	199.52	0.400	0.1045	0.5500	0.6545	5.2610
T6-1	189.63	0.350	0.0733	0.2567	0.3300	3.5001
T6-2	192.61	0.325	0.0764	0.4839	0.5603	6.3308
T6-3	193.10	0.450	0.0973	0.4599	0.5572	4.7266
T6-4	217.47	0.350	0.0853	0.2981	0.3834	3.4947

failure, which is simply by successive delamination along planes parallel to the midplane. This statement can be used to explain partially the impact response of some specimens with large propagation energy, E_p. From Table II, the residual stress free specimens T4-2 and T6-3 show significantly higher absorption energy than the specimens T4-1 and T6-1 with yield tensile residual stresses in the matrix. The lower impact energy mode is caused by the larger tensile matrix

residual stresses. This can be demonstrated by observing the side fracture surface of the specimens (see Fig. 2). The differences in the macrographs of the fracture surfaces in Fig. 2 clearly show the influence of residual stress on the impact response of the present composite materials. With large matrix tensile stress, the fracture is planar but with near free or large compressive matrix stresses, more shear fracture is observed.
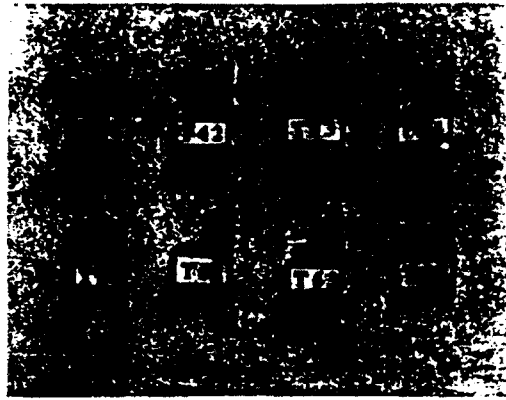
1371

Figure 2 Side fracture surfaces with T4 and T6 treatments

It has been argued by Jang *et al.* [23]. that the matrix should be the dominant factor with only a small amount of fibre breakage prior to maximum loading. Near the maximum loading and soon after that. fibre breakage dominates. This suggests that extensive fibre breakage occurs at the end of the initiation phase of the impact loading. The considerable tensile residual stress in the matrix can promote the initiation stage of fracture at the crack tip to reduce the maximum impact loading of composite materials. Fig. 3 indicates the effect of matrix residual stress on carrying load. As the strain increases. the crack tip, the tensile yielded matrix no longer will carry additional load. resulting in excess stress in the fibre. This leads to fibre breakage in a colinear manner with the crack resulting in the planar fracture surface shown in Fig. 4. When the matrix has a compressive yield residual stress. it can carry a significant fraction of the load at the crack tip and the fibres which are in a tensile residual stress condition will fracture noncolinearly with cracking. The net result is a great deal of shear deformation and fibre pull-out along the continuous fracture path (Fig. 5). For intermediate residual stress level. a mixture of the two failure mechanisms was observed. All the above would be equally true for T4 and T6 treatments.

3.3. Microstructural failure analysis
In general. the possible operating microfailure mechanisms during impact loading include matrix cracking. fibre-matrix debonding. fibre breakage. and fibre pull-out. The work of fracture includes (i) a small contribution from the fracture energy of fibre and matrix. (ii) the debonding energy and (iii) the pull-out energy. From the studies by Kelly [24] and Outwater etc. [25]. it is shown that the work done on separating fibres and matrix can make a major contribution to the total energy of fracture. The mechanism of pull-out is a more significant one than the debonding mechanism as an energy absorber. However. debonding must occur before pull-out. but can be a result of noncolinear fibre breakage. These observations are in agreement with the impact test of the matrix tensile residual stress specimens which have the lowest max-
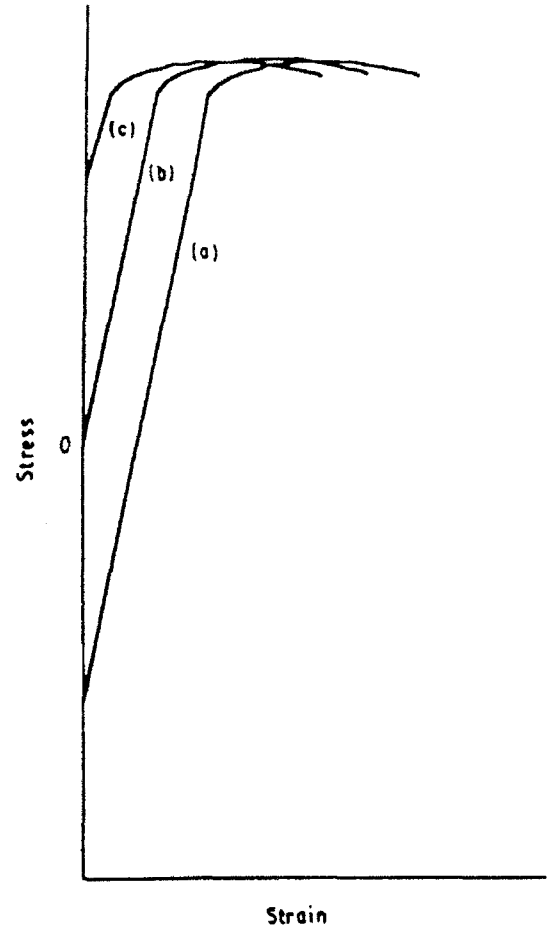

Strain

Figure 3 Matrix residual stress effect on the matrix stress-strain curve (a) compressive residual stress: (b) free residual stress. (c) tensile residual stress.

Figure 4 Fracture surface of specimen T6-1

imum loading and initiation energy. The micrographs of T6-1 and T4-1 specimens have similar fracture pattern as shown in Fig 4. on the microstructural level. The fracture surface is planar. Owing to the matrix yield tensile residual stress effect as discussed previously. the fibres break before extensive separation of the fibres from the matrix leading to a smaller amount of pull-out and thus less absorbed energy [24, 25].
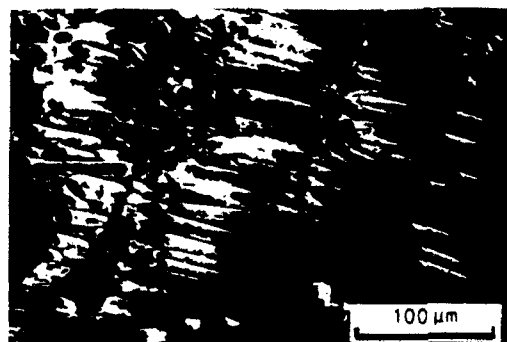
1372

Figure 5 Fracture surface of specimen T4-4

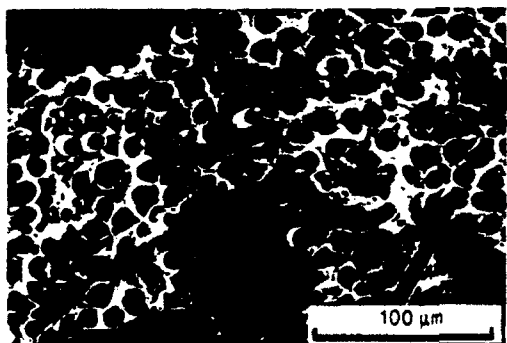*Figure 6* Fracture surface of specimen T6-4

Figure 7 Fracture surface of specimen T4-2.

On the contrary. the specimen T4-4 with large compressive matrix residual stress has a stepwise fracture surface shown in Fig. 5. As described earlier. the matrix can carry some of the applied load. Meanwhile the fibre tensile stress will increase until the matrix reaches the yield stress state. Just as shown in Fig. 3, the fracture strain of T4-4 is larger than that with yield tensile residual stress in the matrix. From the viewpoint of statistics. the possibility of fibre breakage at various positions will increase and produce noncolinear fibre breakage in the fracture surface. This results in a great deal of shear deformation and fibre pull-out. The force time impact response diagram of specimen T4-4. shown in Fig. 1b. also indicates the stepwise fracture mechanism.

The micrographs of specimens T4-3, T6-2 and T6-4 with intermediate residual stresses show a mixture of the two failure mechanisms. a planar fracture surface and a stepwise fracture surface. There are some long pull-out fibres on less planar fracture surfaces which can be observed in Fig. 6. This indicates that debonding and pull-out mechanisms play some roles in the fracture processes and probably result in an increase of impact energy. For the nearly free residual stress specimens T6-3 and T4-2 (Fig. 7), dimple-like fracture surfaces with relatively short fibres extruding are observed. The appearance seems to lie between the two extremes of planar and shear deformed fracture surfaces.

4. Conclusions

Several important conclusions can be drawn. First. the specimen with yield tensile matrix residual stress has a planar fracture surface and low impact energy due to the yield tensile residual stress. Secondly. the specimens with higher compressive matrix residual stress have largest maximum load of all the same matrix treatment specimens. The specimen T4-4 with matrix compressive yield residual stress has the maximum impact energy owing to a stepwise fracture mechanism. Thirdly. specimens with relatively small residual stress have moderate impact energy because of a mixture of failure mechanisms of planar and stepwise fracture surfaces. Finally. it can be concluded that good impact properties of composite materials can be obtained by selecting an appropriate thermal treatment so that the deleterious tensile residual thermal stress can be reduced or even eliminated.

References

1. S D TSAI, D MAHULIKAR, H L MARCUS, I C NOYAN and J B COHEN *Mater. Sci. Engng* 47 (2) (1981) 145

2. S S HECKER, C H HAMILTON and L J EBERT *J Mater JMLS* 4 5 (1970) 868

3. M VEDULA, R N PANGBORN and R A QUEENEY *Composites* 19 (1988) 55

4. Idem. ibid 19 (1988) 133

5. Y H PARK and H L MARCUS in "Mechanical behavior of metal matrix composites". edited by J E Hack and M F Amateau. Conference Proceedings of the Metallurgical Society of AIME and the Material Science Division of ASM (American Institute of Mining. Metallurgical. and Petroleum Engineerings. New York. 1983) pp 77 81

6. C N J WAGNER, M S BOLDRICK and V PEREZ-MENDEZ *Adv X-Ray Anal* 26 (1982) 275

7. E MACHERAUCH and U WOLFSTIEG ibid 20 (1977) 369

8. V M HAUK, R W M OLDELHOVENS and G J H VAESSEN *Metall Trans* 13A (1982) 1239

9. K WAKASHIMA, T KAWAKIBO and S UMEKAWA ibid 6A (1975) 1755

10. J. D. WINKEL and D. F. ADAMS *Composites* **16** (1985) 268.

11. C. K. L. DAVIES, S. TURNER and K. H. WILLIAMSON *ibid.* **16** (1985) 279.

12. S. L. KESSLER, G. C. ADAMS, S. B. DRISCOLL and D. R. IRELAND (eds), Instrumented Impact Testing of Plastics and Composite Materials, ASTM STP 936 (American Society for Testing and Materials, Philadelphia, 1987).

13. J. S. WU, K. FRIEDRICH and M. GROSSO *Composites* **20** (1989) 223.

14. M. N. GHASEMINEJHAD and A. PARVIZI-MAJIDI *ibid.* **21** (1990) 75.

15. H. S. PARK, Doctoral dissertation, University of Texas, Austin, TX (1989).

16. H. S. PARK, J. L. DOONG and H. L. MARCUS, submitted to *J. Mater. Sci. Engng.*

17. M. H. RICE, A. MAEWAL and G. A. GURTMAN, "The effects of residual stresses on the X-Ray induced response of metal matrix composites", DNA report (SSS-FTR-89-10219), 1989.

18. H. M. LEDBETTER and M. W. AUSTIN, in "Residual Stress in Science and Technology", edited by E. Macherauch and V. Hauk, International Conference on Residual Stresses, 1986, Garmisch-Partenkirchen, FRG, 1987, DGM Informations-gesellschaft, Germany, pp. 517-22.

19. Y. IKUTA, CHU and H. FUJIWARA, *ibid.* pp. 523-30.

20. H. GRAY, J. WAGNER and G. TIERING, *ibid.* pp. 815-22.

21. J. L. DOONG, T. J. CHEN and Y. H. TAN *Engng Fract. Mech.* **33** (1989) 483.

22. A. GOLOVOY, M. F. CHEUNG and H. van OENE, "The impact behaviour of glass and carbon fiber composites", Ford Research Technical Report SR-86-136, Ford Motor Co., Dearborn, MI (1986).

23. B. Z. JANG, L. C. CHEN, T. R. HWANG, J. E. HAWKES and R. H. ZEE *Polym. Compos.* **11** (1990) 144.

24. A. KELLY *Proc. R. Soc. Lond.* **A319** (1970) 95.

25. J. O. OUTWATER and M. C. MURPHY, "Fracture energy of unidirectional laminates", Proceedings of the 24th SPI RP Conference, paper 11-B (Society of the Plastics Industry, New York, 1969).